Modelling of soot coalescence and aggregation with a two-population balance equation model and a conservative finite volume method

Binxuan Sun, Stelios Rigopoulos*, Anxiong Liu[1]

Department of Mechanical Engineering, Imperial College London, South Kensington Campus, London SW7 2AZ, UK

Abstract

The objective of the present paper is to develop a population balance approach for modelling soot formation that distinguishes between coalescence and aggregation and accounts for finite-rate fusing of primary particles within aggregates, while providing a numerically accurate description of primary particle surface growth and oxidation within aggregates. To this end, the recently developed conservative finite volume sectional method for the solution of the population balance equation (PBE) due to Liu and Rigopoulos (2019, Combust. Flame 205, 506-521) is extended to a two-PBE approach that allows for a more accurate modelling of primary particle surface growth and oxidation and furthermore involves a timescale for the fusing of primary particles. The accuracy of the numerical method is first tested by calculating the self-preserving distributions of aggregates with varying fractal dimension. Subsequently, the one-PBE and two-PBE approaches are coupled with CFD and applied to the simulation of the Santoro laminar non-premixed co-flow sooting flame. The results show that both approaches can provide good prediction of the soot volume fraction, but the two-PBE approach yields a significant improvement in the prediction of soot morphology. At present, the information available for modelling the gradual fusing of soot primary particles is based on experiments on silica and titania nanoparticles, and therefore a comprehensive study of the impact of the sintering model parameters is conducted. Finally, conclusions are drawn regarding the predictive potential of the one-PBE and two-PBE approaches.

Keywords: Soot, population balance, sectional method, fractal aggregates, sintering, CFD

1. Introduction

The reduction of soot emissions in combustion processes is a primary concern of combustion engineers due to the severe health impact of soot. Particles of different sizes have different impacts on human health;

*Corresponding author

Email address: s.rigopoulos@imperial.ac.uk (Stelios Rigopoulos)

[1]Present address: Department of Mechanical Engineering, University College London, Torrington Place, London WC1E 7JE, UK

small particles, in particular, penetrate into the lungs with severe adverse effects, and increasingly stringent regulations thus place importance on the prediction of the soot particle size distribution (PSD). Soot comprises both spherical primary particles and fractal aggregates, and the prediction of its morphology is also important because a) it affects the aggregate surface area, which in turn affects the rates of surface growth and oxidation, b) it affects the aggregate size, and c) it has an effect on the optical properties of soot that can be measured. Furthermore, the control of PSD and morphology is of primary importance in the gas-phase synthesis of functional nanoparticles, because it allows tailoring the particles to particular applications [1]. The PSD can be predicted by solving the population balance equation (PBE), which describes the evolution of the PSD due to kinetic processes such as nucleation, growth and aggregation, as well as transport processes, while several approaches have been proposed for introducing morphology in the PBE. Furthermore, the PBE must be coupled with fluid dynamics, species transport and chemical kinetics in order to predict the soot properties in laminar and turbulent flames. Finally, accurate and computationally efficient methods must be employed for solving the CFD-PBE approach.

The PBE is a partial integro-differential equation that requires specialised methods for its solution. Analytical solutions are available only for special cases, while Monte-Carlo methods have been employed mostly in ideal reactors or one-dimensional laminar flames [2, 3]. For more complex two- and three-dimensional flows, the families of methods that have been employed are moment and discretisation (also called sectional) methods. In moment methods (Refs. [4–6] among others), one solves for the moments of the distribution, rather than for the PSD, and therefore the number of variables is kept to a minimum. However, moment methods do not predict the PSD, and furthermore the moment equations are unclosed, thus requiring closure assumptions. Sectional methods, on the other hand, solve directly for the PSD and do not require closure assumptions, but the discretisation of the PBE poses several unique challenges due to the presence of integral terms, thus requiring the development of specialised methods. The progenitor of sectional methods is the approach proposed by Bleck [7] in aerosol science, where a graphical procedure was used to illustrate the particle sectioning. The approach of Gelbard et al. [8], also initially developed for atmospheric aerosols, was later applied to soot formation in laminar premixed [9] and diffusion flames [10–12]. This implementation is, however, restricted in terms of the grid employed. The approach of Kumar and Ramkrishna [13] originates in the chemical engineering literature and has also been employed for soot formation in several studies, such as Refs. [14, 15]. This approach is not limited by the choice of grid and represents the distribution as a sum of delta functions, such that only certain particle sizes are allowed. Since a non-uniform grid cannot account for all aggregates formed, as they may not lie at grid nodes, correction factors are introduced to conserve any two moments by distributing the moments of aggregates to the two adjacent points. However, this approach places a priority on moment conservation at the expense of accuracy in the prediction of the distribution. Adaptive grid approaches have also been developed and applied to aerosols and soot [16–19]. Liu and Rigopoulos [20] recently proposed a finite volume method that combines accurate prediction of the

distribution with moment conservation in an arbitrary grid. A more extensive recent review of solution methods for the PBE with focus on soot modelling has been provided by Rigopoulos [21].

An important challenge in the population balance modelling of soot formation is the prediction of soot morphology. Once two particles have collided, the aggregate gradually transforms towards a spherical shape via the process known as sintering in materials science. As the fusing of soot particles involves different physical mechanisms, different terms such as coalescence and aggregation have been suggested for use in the soot literature [22]. Incipient liquid-like particles are subjected to instantaneous coalescence to form spherical particles. Larger primary particles form aggregates with fractal shapes, within which they are gradually being fused. The present paper addresses the question of how to account for aggregate morphology in the formulation and solution of population balance models. Three concepts have appeared in the literature for extending the PBE to account for fractal aggregates, and these will be described in the following discussion.

The first approach is to employ the standard PBE with different aggregation kernels for spherical particles and aggregates, and to impose a cut-off size that separates the two types. This formulation can be solved with standard sectional methods and has been used in many studies, including Refs. [20, 23–26]. There are, however, two important limitations associated with this approach. The first one is related to the model parameter, the cut-off size, which is an artificial conception that does not represent the physics of aggregation, assuming as it does instantaneous coalescence up to a considerable size and no further fusing afterwards. As mentioned, only very small particles coalesce instantaneously, while larger particles are fused with a finite timescale. The second limitation is related to the calculation of surface growth and oxidation, which is carried out in an inconsistent manner in the context of this approach. The size of the primary particles is assumed to be frozen once they reach the cut-off size, in spite of the fact that growth and oxidation continue to take place. Therefore the surface area, on which these processes depend, is inconsistent with the rate of change of the particle volume.

The second approach is the two-dimensional PBE proposed by Koch and Friedlander [27]. In this approach, the particle surface area is introduced as an additional independent variable in the PBE, and an additional term is introduced to account for sintering. A two-dimensional sectional method for the numerical solution of this formulation was developed and applied to the study of silica and titania nanoparticles by Xiong and Pratsinis [28] and Xiong et al. [29]. This approach is the most comprehensive one, but it is computationally expensive due to the two dimensions involved. While its employment in the context of an ideal reactor or a one-dimensional flame is affordable, its coupling with a three-dimensional CFD simulation would require excessive resources.

The third approach is to employ an additional dependent, rather than independent, variable, resulting in a system of coupled PBEs. This approach was pioneered by Rogak [30] and Tsantilis and Pratsinis [31], initially to describe the aerosol synthesis of nanoparticles such as silica and titania. The first of these studies employed an additional discrete PBE for the number of primary particles in the aggregates, while

sintering was assumed to be instantaneous for particles smaller than a critical diameter. The second study employed an additional PBE for the aggregate surface area. The equation for the evolution of the surface area due to sintering is the same as the equation employed in the two-dimensional formulation. In the two-PBE approach, however, an average surface area is considered for each particle size section, in contrast to the two-dimensional PBE. In the work of Xiong and Pratsinis [28], where a sectional method was used to discretise the two-dimensional PBE, the effect of the number of surface area sections within a size section on the grain size predicted was found to be less than 5%. The two-PBE approach is computationally economic and suitable for coupling with CFD. Further studies with this approach on nanoparticle synthesis (silica and/or titania) employed either the surface area equation [32] or the number of primary particles [33, 34]. The method was also applied to soot [35–39] with the number of primary particles being the second equation.

There are several outstanding questions, however, regarding the two-PBE approach. The theoretical advantages over the one-PBE approach, which is customarily employed in turbulent flow simulations, and the sensitivity of the key parameters must be systematically investigated in laminar flames where reliable datasets are available and where the interaction between turbulence, chemistry and soot does not complicate matters further. The gradual fusing of primary particles that shapes the surface area of aggregates has rarely been studied in soot modelling, although it is employed in the modelling of silica and titania nanoparticle formation. Recently, Chen et al. [40] employed the sintering expression for SiO_2 in the context of a Monte-Carlo simulation of soot formation in laminar ethylene premixed flames, where the sintering parameters were adjusted to match soot experiments. On the other hand, Veshkini et al. [39] employed an expression originating in TiO_2 particles in the context of a sectional method for a sooting laminar diffusion flame. Since there is no experimental information on the rate of fusing of soot primary particles, however, the extrapolation of kinetics extracted from other inorganic nanoparticles warrants a systematic investigation. Finally, the structure and performance of numerical methods for the solution of two-PBE models must be analysed. In a problem as complex as soot formation in flows, establishing the accuracy of numerical methods is essential for preventing compensation of modelling and numerical errors.

The objective of this work is twofold. The first objective is to extend the conservative finite volume method for the solution of the PBE proposed by Liu and Rigopoulos [20], originally formulated for a single PBE (CFV-1PBE), to a two-PBE formulation (CFV-2PBE) that distinguishes between coalescence and aggregation and accounts for finite-rate fusing of primary particles within aggregates, while at the same time providing a consistent and numerically accurate description of primary particle surface growth and oxidation within aggregates. The second objective is to conduct a systematic study of the two-PBE approach, by comparing it with the one-PBE approach and investigating the effect of key parameters related to the evolution of soot morphology in both cases. To accomplish these objectives, the extended method is first shown to reproduce the self-preserving distributions correctly in the two asymptotic cases of coalescence into spherical particles and aggregation into fractal aggregates. The method is then coupled with a CFD

code and applied to the modelling of the laminar co-flow diffusion flame of Santoro et al. [41]. Apart from comparison with experimental results, an analysis of the effect of key parameters is conducted, which allows a discussion of the potential and limitations of the one-PBE and two-PBE approaches.

2. The one-PBE model of aggregation and the conservative finite volume method

In this section, we summarise the concepts underlying the CFV-1PBE method. As the numerical aspects have been described in Ref. [20], the emphasis here is on explaining its deficiencies when it comes to the modelling of fractal aggregates.

The CFV-1PBE method is a finite volume method for the solution of the one-dimensional PBE with nucleation, condensation, growth (or oxidation) and aggregation. For a spatially homogeneous system, the equation is shown below (the coupling with flow will be discussed later):

$$\frac{\partial n}{\partial t} + \frac{\partial (G(v,\mathbf{Y})n)}{\partial v} = B\delta(v-v_0) + C(\mathbf{Y},v) + \frac{1}{2}\int_0^v \beta(w,v-w)n(w,t)n(v-w,t)dw - n(v,t)\int_0^\infty \beta(v,w)n(w,t)dw \quad (1)$$

where B, G, and C are the nucleation, growth and condensation rates, respectively, and $\beta(v,w)$ is the aggregation kernel (the models for these processes will be discussed in Sec. 5). The objectives of this method are to attain: a) accurate prediction of the distribution with a small number of sections, b) conservation of the first moment (or any other single moment) in aggregation, c) applicability to any non-uniform grid (even an adaptive one), and d) speed and robustness for coupling with CFD. The method is based on the framework of finite volume methods, which are endowed with the conservation property by balancing the inflow and outflow fluxes. In the PBE, however, due to the presence of the integral terms, the fluxes originate in various parts of the domain, and furthermore the form of the aggregation birth term (which resembles a convolution) makes it difficult to distinguish between the fluxes originating from different subdomains. In this method, a transformation is used to decompose the birth term into its constituent fluxes and a map is constructed to record them. An important part of the method is the algorithm for constructing this map in an arbitrary non-uniform grid. The aggregation birth and death terms are then calculated via these fluxes, and the conservation of mass is ensured without introducing correction terms. The map is constructed at the beginning and accessed during the simulation, and the method is thus computationally efficient and easy to couple with CFD. Test cases, including analytical solutions and a co-flow laminar flame [20], have shown that the method produces very accurate solutions that conserve the first moment, even on coarse grids.

When it comes to the modelling of aggregation, the previous applications of the CFV-1PBE method [20, 26] employed the first of the three approaches mentioned in Sec. 1, which is to impose a cut-off size between spherical particles and fractal aggregates and assume that aggregates are composed of a number of equally sized primary particles. In this approach, the only modification needed in Eq. 1 in order to account for

aggregation is to formulate the aggregation kernel in terms of the aggregate collision diameter, d_g, which is related to the volume of the aggregate v via the following equation [42]:

$$\frac{v}{v_p} = k_f \left(\frac{d_g(v)}{d_p} \right)^{D_f} \tag{2}$$

where v_p and d_p are the volume and diameter of the primary particles, respectively, k_f is the fractal prefactor and D_f is the fractal dimension. The latter has the value 3 for spherical particles and 1 for linear ones, with fractal aggregates having values in between. A constant fractal dimension is usually assumed in population balance models (see e.g., Refs. [35, 43, 44]), based on observations from experiments (see e.g., Refs. [45–48]) that the fractal dimension of aggregates exhibits values around 1.8. Spherical particles can exhibit a range of diameters up to the cut-off size, while all primary particles within aggregates are assumed to have a diameter d_p equal to the cut-off size. The implementation of aggregates in the context of the CFV-1PBE method is thus straightforward, as no modifications in the overall structure of the PBE are involved. As mention in Sec. 1, however, this approach has two significant limitations: the need to specify a cut-off size, which is an artificial and non-physical parameter, and the inconsistent calculation of the rate of surface processes, i.e. growth and oxidation. These limitations originate in the fact that the one-dimensional PBE is inherently inadequate to provide an accurate description of aggregates due to the lack of morphological variables in the formulation.

3. The two-PBE model of aggregation

To provide a consistent and physical account of aggregation, the population balance model must address the two limitations mentioned at the end of the last section. The introduction of an additional variable, rather than a parameter such as the cut-off point, is essential to account for aggregate morphology. As discussed in Sec. 1, both surface area and the average number of primary particles per aggregate have been employed as the second variable for describing aggregate morphology, and the latter approach is employed in this work.

A schematic illustration of the concepts underlying the one-PBE and two-PBE models is shown in Fig. 1. Note that it is still necessary to distinguish between the coalescence of incipient particles, which is virtually instantaneous, and the gradual fusing of primary particles within aggregates. While a critical diameter is employed in both models, its impact in the one-PBE model is far greater, as all primary particles within aggregates are assumed to have this diameter, while in the two-PBE model it just distinguishes the incipient particles from the rest. If the same critical diameter is employed in both models and no finite-rate fusing is introduced in the two-PBE model, both models would yield the same self-preserving distribution (as shown later in Sec.6, Fig. 5). The determination of this diameter will be addressed in Section 5.5.

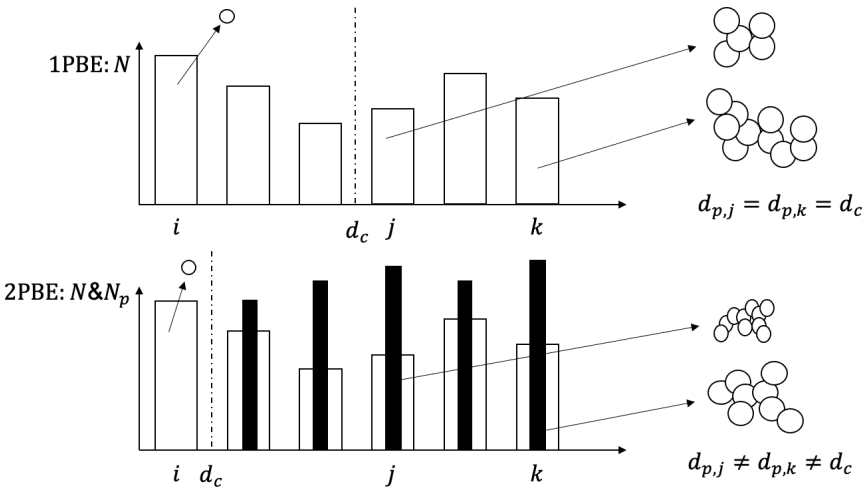


Figure 1: A schematic illustration of the concepts involved in the one-PBE and two-PBE models. The white histogram represents number of aggregates, while the black histogram represents number of primary particles.

The first equation of the model is the PBE for the number density of soot particles, whether primary ones or aggregates, with the addition of transport in physical space:

$$\frac{\partial n}{\partial t} + \frac{\partial (G(v,\mathbf{Y})n)}{\partial v} + \frac{\partial (u_j n)}{\partial x_j} = \frac{\partial}{\partial x_j}\left(D_p \frac{\partial n}{\partial x_j}\right) + B(\mathbf{Y})\delta(v - v_0) + C(v,\mathbf{Y}) + \frac{1}{2}\int_0^v \beta(w, v-w)n(w)n(v-w)dw - \int_0^\infty \beta(v,w)n(v)n(w)dw \quad (3)$$

where D_p denotes the particle diffusion coefficient, which is size-dependent [42]. In this and the following equations, the dependence on v, $\mathbf{x}$ and t will be omitted except when necessary. This equation is coupled with the equations of fluid dynamics and species transport equations via the velocity field, u_i, and the concentrations of chemical species, Y_α. Two issues must be addressed when fractal aggregates are present: the aggregation kernel must be formulated in terms of their collision diameter, and the calculation of the surface area, which appears in the growth function, must take into account the structure of the aggregates. The first issue is straightforward, as the aggregate collision diameter can be related to the aggregate volume via Eq. 2; it must be noted that, unlike the case of the one-PBE model, the average primary particle volume does not remain constant here. The second issue is the source of the inconsistent calculation of growth in the one-PBE model and will be addressed via the second PBE, in the context of which we will introduce the finite-rate fusing of primary particles.

The second equation is the PBE for the number density of primary particles. We denote by $n_{av}(v,t)$ the average number of primary particles per aggregate having volume v at time t:

$$n_{av}(v,t) = \frac{n_p(v,t)}{n(v,t)} \quad (4)$$

where $n_p(v,t)$ represents the number density of primary particles that form aggregates of volume v. Ac-

cording to Eq. 2, this can be related to the collision diameter d_g as follows:

$$n_{av}(v,t) = k_f \left(\frac{d_g(v)}{d_p(v)}\right)^{D_f} \tag{5}$$

The gradual fusing of primary particles within an aggregate results in a change in surface area, a, according to the following equation formulated by Koch and Friedlander [27]:

$$\frac{da}{dt} = -\frac{1}{\tau_s}(a - a_s) \tag{6}$$

where τ_s denotes the characteristic timescale. Eq. 6 expresses the fact that the driving force for fusing is the deviation of the surface area of an aggregate from that of a sphere with equal volume, a_s. It is now possible to obtain an equation for the rate of change of the primary particles, as shown in Ref. [33]. Considering an aggregate composed of n_p spherical primary particles of radius r, its volume v and surface area a have the following expressions:

$$v = n_p v_p = \frac{4\pi}{3} n_p r^3 \tag{7}$$

$$a = n_p a_p = 4\pi n_p r^2 \tag{8}$$

where a_p is the surface area of a primary particle. Using Eqs. 7 and 8, the surface area a can be expressed in terms of v and n_p as follows:

$$a = \left(36\pi v^2 n_p\right)^{1/3} \tag{9}$$

As the volume of the aggregate does not change during the fusing of primary particles, Eq. 9 can be differentiated to obtain:

$$\frac{da}{dt} = \left(\frac{\frac{4}{3}\pi v^2}{n_p^2}\right)^{1/3} \frac{dn_p}{dt} \tag{10}$$

Similarly, the surface area of the sphere with equal volume can be expressed in terms of v as:

$$a_s = \left(36\pi v^2\right)^{1/3} \tag{11}$$

At this point, by substituting Eq. 9 and Eq. 11 into Eq. 6 and replacing da/dt with the aid of Eq. 10, we can derive the following expression:

$$\frac{dn_p}{dt} = -\frac{3}{\tau_s}\left(n_p - n_p^{2/3}\right) \tag{12}$$

Finally, the rate of change of the average number of primary particles per aggregate due to fusing can be obtained as follows [33]:

$$\left.\frac{dn_{av}}{dt}\right|_f = -\frac{3}{\tau_s}\left(n_{av} - n_{av}^{2/3}\right) \tag{13}$$

The derivation of the aggregation term for primary particles is based on the following consideration: the increase in the number of primary particles of size v due to the collision must account for the primary particles originating from both particle $v-w$ and w, and the aggregation terms for n_p can thus be written in

terms of n and n_{av}. The PBE for the primary particles, including transport terms, can therefore be written as follows:

$$\frac{\partial n_p}{\partial t} + \frac{\partial \left(G(v,\mathbf{Y})n_p\right)}{\partial v} + \frac{\partial (u_j n_p)}{\partial x_j} = \frac{\partial}{\partial x_j}\left(n_{av} D_p \frac{\partial n}{\partial x_j}\right) - \frac{3}{\tau_s}\left[\frac{n_p}{n} - \left(\frac{n_p}{n}\right)^{2/3}\right] n + C_p(v,\mathbf{Y}) + \frac{1}{2}\int_0^v \beta(w, v-w) n(w) n(v-w)(n_{av}(v-w) + n_{av}(w)) dw - \int_0^\infty \beta(v,w) n(w) n(v) n_{av}(v) dw \quad (14)$$

As mentioned, the coalescence of incipient particles is assumed to be instantaneous, hence Eq. 14 is invoked only for sections where the particle diameter exceeds the critical diameter.

4. The conservative finite volume method for the two-PBE model (CFV-2PBE)

In this section, we will show how the CFV-1PBE method can be extended to the two-PBE model. The number density distribution of particles in the volume section (v_{i-1}, v_i) (referred to as section i in the following) is assumed to be uniform and will be written as N_i for aggregates and $N_{p,i}$ for primary particles, while the corresponding average number of primary particles per aggregate will be denoted as $n_{av,i}$.

4.1. Nucleation and growth

The finite volume discretisation for the nucleation and growth terms in the PBE for the aggregates can be written as follows:

$$\left.\frac{dN_i}{dt}\right|_{nuc,gr} = -\frac{1}{\Delta v_i}\left[nG(v,\mathbf{Y})\right]\Big|_{v_{i-1}}^{v_i} + \frac{1}{\Delta v_i}\int_{v_{i-1}}^{v_i} B_i dv_i \quad (15)$$

where the nucleation rate, B_i, is non-zero only over the interval including the nuclei volume v_0. For primary particles, the growth term is formulated as follows:

$$\left.\frac{dN_{p,i}}{dt}\right|_{gr} = -\frac{1}{\Delta v_i}\left[n_p G(v,\mathbf{Y})\right]\Big|_{v_{i-1}}^{v_i} \quad (16)$$

No nucleation term is included in the equation for $N_{p,i}$, as this PBE is solved only for particles greater than the critical diameter where coalescence is not instantaneous.

The treatment of the growth term in the two-PBE model must be guided by the principle that the growth of primary particles is related to that of aggregates, and thus an identical growth rate must be employed. For example, when an aggregate enters section $i+1$ from section i, all of the primary particles within that aggregate will also enter section $i+1$. Assuming that an aggregate experiences only surface growth, the aggregate volume increases while the number of primary particles maintains the same, leading to an increased primary particle size. Hence the model provides a consistent description for the growth, compared to the one-PBE model that was based on the assumption of constant primary particle size. Therefore, the finite volume discretisation for the growth term is identical in both PBEs and need to be computed only once. It will be shown below for the aggregate PBE, using a total variation diminishing (TVD) scheme that

is due to Koren [49] and first employed in the context of the PBE by Qamar et al. [50, 51] for an arbitrary non-uniform grid:

$$(nG(v,\mathbf{Y}))_{v_i} = G(v,\mathbf{Y})\left[N_{u(v_i)} + \frac{1}{2}\phi(r_i)\left(N_{u(v_i)} - N_{uu(v_i)}\right)\right] \tag{17}$$

where the $N_{u(v_i)}$ and $N_{uu(v_i)}$ are the number densities of the two cells upstream of node v_i and $\phi(r_i)$ is the flux limiter at node v_i [52]:

$$\phi(r_i) = \max\left[0, \min\left[2r_i, \min\left(\frac{1}{3}\frac{v_i - v_{i-1}}{v_{m,i} - v_{m,i-1}} + \frac{2r_i}{3}\frac{v_i - v_{i-1}}{v_{m,i+1} - v_{m,i}}, 2\right)\right]\right] \tag{18}$$

In this equation, $v_{m,i} = 0.5(v_i + v_{i-1})$ and r_i is the upwind ratio of two consecutive number density gradients [49]:

$$r_i = \frac{N_{i+1} - N_i + \epsilon}{N_i - N_{i-1} + \epsilon} \tag{19}$$

where ϵ is a small number employed to avoid division by zero.

The growth rate depends on the surface area of soot aggregates, which is calculated as follows [46]:

$$a_i = a_{(C_{ov}=0),i}\left[1 - \phi C_{ov}\left(1 - \frac{1}{n_{av,i}}\right)\right] \tag{20}$$

where $\phi = 1.3$ denotes the averaged number of contacts per primary particle, C_{ov} is the overlap parameter for which the value 0.15 is used [46] and $a_{(C_{ov}=0)}$ denotes the surface area of the aggregates when there is no overlap between primary particles (point contact).

4.2. Aggregation

In the CFV-1PBE method, the discretisation of the aggregation terms can be written as follows:

$$\begin{aligned}\left.\frac{dN_i}{dt}\right|_{agg} = &\frac{1}{\Delta v_i}\int_{v_{i-1}}^{v_i}\int_{v_0}^{\frac{v}{2}}\beta(w, v-w)n(w)n(v-w)dwdv \\ &- \frac{1}{\Delta v_i}\int_{v_{i-1}}^{v_i}\int_{v_0}^{v_{max}}\beta(v,w)n(v)n(w)dwdv\end{aligned} \tag{21}$$

The main challenge addressed by this method is the evaluation of the double integrals for an arbitrary non-uniform grid. The details of how this is carried out and the final discretised equations can be found in Ref. [20].

To extend the method to the two-PBE model, we need evaluate the corresponding terms for the equation for the primary particle number density. We consider a case where a particle at interval j collides with a particle at interval k forming a new particle at interval i. The change in the number of aggregates dN_i and the change in the number of primary particles $dN_{p,i}$ are then related as follows:

$$dN_i = -dN_j = -dN_k \tag{22}$$

$$dN_{p,i} = -n_{av,j}dN_j + -n_{av,k}dN_k \tag{23}$$

The change in primary particle number density $dN_{p,i}$ can thus be extracted from the aggregation term in the PBE for the aggregates, and no further calculation is needed.

4.3. Fusing of primary particles

The discretised form of the term corresponding to the fusing of primary particles in the PBE for the primary particles can be derived from Eqs. 4 and 13 in a straightforward manner:

$$\left.\frac{dN_{p,i}}{dt}\right|_f = \left.\frac{dn_{av,i}}{dt}\right|_f N_i = -\frac{3}{\tau_s}\left[\frac{N_{p,i}}{N_i} - \left(\frac{N_{p,i}}{N_i}\right)^{2/3}\right] N_i \tag{24}$$

where the models for the characteristic timescale τ_f will be discussed in Sec. 5.5.

4.4. Coupling with flow

In order to account for transport in physical space, convection and diffusion terms must be introduced into the PBE. For the CFV-2PBE method, the transport equation for the spatially varying number density $N_i(x,t)$ and $N_{p,i}(x,t)$ has the following form:

$$\begin{aligned}\frac{\partial N_i}{\partial t} + \frac{\partial (u_j N_i)}{\partial x_j} &= \frac{\partial}{\partial x_j}\left(D_{p,i}\frac{\partial N_i}{\partial x_j}\right) + S_a \\ \frac{\partial N_{p,i}}{\partial t} + \frac{\partial \left(u_j N_{p,i}\right)}{\partial x_j} &= \frac{\partial}{\partial x_j}\left(n_{av,i} D_{p,i}\frac{\partial N_i}{\partial x_i}\right) + S_p\end{aligned} \tag{25}$$

where all PBE terms apart from spatial convection and diffusion have been grouped into the source terms S_a and S_p, while $D_{p,i}$ denotes particle diffusion for section i. The velocity, u_j, is equal to the sum of the flow velocity, U_j, and the thermophoretic velocity, u_j^t. The latter can be computed from the following equation [42]:

$$u_j^t = -0.55\frac{\mu}{\rho T}\frac{\partial T}{\partial x_j} \tag{26}$$

where μ and ρ are the gas viscosity and density respectively.

It is important to ensure that the flux of the primary particle number density $N_{p,i}(\mathbf{x},t)$ within a volume section i is consistent with that of the aggregate number density $N_i(\mathbf{x},t)$ within the same volume section i. For the convective fluxes, the primary particles experience the same spatial convection as the aggregates and therefore both convective terms share the same velocity. A slightly different treatment is employed for the diffusion of primary particles, $\frac{\partial}{\partial x_j}\left(n_{av,i} D_{p,i}\frac{\partial N_i}{\partial x_j}\right)$, where the term $D_{p,i}\frac{\partial N_i}{\partial x_j}$ is multiplied with $n_{av,i}$. In Appendix A, we show in detail the discretisation scheme for the convection and diffusion of the primary particles and validate it via a simplified test case.

4.5. Complete discretised equations for CFV-2PBE

Assembling all terms, the complete discretised equations for the CFV-2PBE method are:

$$\frac{dN_i}{dt} + \frac{\partial (U_j + u_j^t) N_i}{\partial x_j} = \frac{\partial}{\partial x_j}\left(D_{p,i}\frac{\partial N_i}{\partial x_j}\right) - \left[NG(v,\mathbf{Y})\right]\Big|_{v_{i-1}}^{v_i} + C_i(v,\mathbf{Y}) + \left.\frac{dN_i}{dt}\right|_{agg} + B_i(\mathbf{Y})\delta(v - v_0) \tag{27}$$

$$\begin{aligned}\frac{dN_{p,i}}{dt} + \frac{\partial (U_j + u_j^t) N_{p,i}}{\partial x_j} =& \frac{\partial}{\partial x_j}\left(n_{av,i} D_{p,i}\frac{\partial N_i}{\partial x_j}\right) - \left[N_p G(v,\mathbf{Y})\right]\Big|_{v_{i-1}}^{v_i} + C_{p,i}(v,\mathbf{Y}) \\ & - \frac{3}{\tau_s}\left[\frac{N_{p,i}}{N_i} - \left(\frac{N_{p,i}}{N_i}\right)^{2/3}\right] N_i + \left.\frac{dN_{p,i}}{dt}\right|_{agg}\end{aligned} \tag{28}$$

4.6. Coupling of CFV-2PBE with CFD

The CFV-2PBE model has been implemented in our in-house CFD code BOFFIN [53]. The solution method is based on a second-order finite volume scheme. A fractional step method is employed, with separate fractional steps for convection-diffusion, chemical reaction and PBE. A second-order central difference scheme is applied to the diffusion terms, while a TVD scheme with van Leer's limiter is implemented for the convection terms. For the temporal integration of the convection and diffusion processes, the second-order accurate Crank-Nicolson method is applied. The calculation of the chemical reaction step is performed with a backward Euler method, and a modified Newton-Raphson scheme is implemented for solving the resulting system of non-linear equations. The temporal integration of the discretised PBE is not stiff, and therefore the explicit Euler method is used in the PBE fractional step.

5. Soot kinetics

5.1. Gas-phase chemistry and radiation

A detailed chemical mechanism due to Blanquart et al. [54], is employed in this study. The mechanism was developed with the focus on the important species for soot formation such as acetylene, the C_3H_4 isomers, propene and butadiene. It contains 149 species and 1651 reactions, accounting for the formation of larger PAH species up to cyclopenta[cd]pyrene ($C_{18}H_{10}$). The complete mechanism has been validated for a large set of fuels ranging from methane to iso-octane in laminar premixed and counterflow diffusion flames. Finally, an optically thin radiation model is applied, and the implementation is similar to the one in Ref. [18].

5.2. Nucleation and condensation

The model for soot nucleation and condensation employed in this study is due to Blanquart and Pitsch [55]. In this model, the self-collision of two PAHs forms a dimer, which is an intermediate state between the gaseous polycyclic aromatic hydrocarbons (PAH) and solid soot particles. The dimers are then consumed either by self-coalescence to form soot nuclei or by condensation onto the surface of soot particles. The dimerisation of eight PAHs, from naphthalene ($C_{10}H_8$) up to cyclopenta[cd]pyrene, ($C_{18}H_{10}$) is considered. The self-collision rate, $\omega_{\mathrm{PAH},i}$, for a certain PAH_i is given by the following expression:

$$\omega_{\mathrm{PAH},i} = \gamma_i \sqrt{\frac{4\pi k_{\mathrm{B}} T}{m_i}} d_{\mathrm{PAH},i}^2 [\mathrm{PAH}]_i^2 {N_{\mathrm{A}}}^2 \tag{29}$$

where γ_i is the sticking coefficient factor for PAH_i, N_{A} is the Avogadro number, k_{B} is the Boltzmann constant, m_i is the mass of the particle PAH_i, T is the gas temperature and $d_{\mathrm{PAH},i}$ is the diameter of a PAH_i particle given by the following expression [56]:

$$d_{\mathrm{PAH,i}} = D_{\mathrm{A}} \sqrt{\frac{2n_{c,i}}{3}} \tag{30}$$

where D_A is the size of a single aromatic ring of $1.395\sqrt{3}$ Å and $n_{c,i}$ is the number of C atoms in a PAH_i molecule. The PAHs involved in the dimerisation and their corresponding parameters can be found in Table 1 of Ref. [55].

Because of the small size of the PAH molecule, an average volume v_dimer is used to represent the different volume of dimers produced by the self-collision of the eight PAHs ($m = 8$):

$$v_\mathrm{dimer} = \frac{\sum_{i=1}^{m} \omega_{\mathrm{PAH},i} 2 v_{\mathrm{PAH},i}}{\sum_{i=1}^{m} \omega_{\mathrm{PAH},i}} \tag{31}$$

where m is the number of PAHs considered. Note that v_dimer will vary in the calculation depending on the local PAHs concentration. The dimers are assumed to be in a quasi-steady state as a result of the high collision frequency with other dimers or soot particles. Consequently, their production and consumption rates are equal and a quadratic equation of the following form is solved to obtain the dimer concentration:

$$a_{nuc}[\mathrm{dimer}]^2 + b_{cond}[\mathrm{dimer}] = \sum_{i=1}^{m} \omega_{\mathrm{PAH},i} \tag{32}$$

The coefficients a_{nuc} and b_{cond} are determined by the dimer consumption due to nucleation and condensation respectively, and the expressions that yield them will be shown in the following discussion. The positive root of Eq. 32 is accepted as the dimer concentration.

Coalescence of two dimers leads to the formation of soot nuclei [55]. The nucleation rate, w_{nuc}, takes the following form:

$$w_{nuc} = E_F \left(\frac{3}{4\pi}\right)^{1/6} \sqrt{\frac{6 k_\mathrm{B} T}{\rho_s}} 4\sqrt{2} v_\mathrm{dimer}^{1/6} [\mathrm{dimer}]^2 {N_\mathrm{A}}^2 \tag{33}$$

where $E_F = 2.2$ is the Van der Waals enhancement factor [57] and $\rho_s = 1800$ kg/m^3 is the density of soot particle. Thus, the nucleation source term B in Eq. 1 is written as:

$$B = w_{nuc} \frac{2 v_\mathrm{dimer}}{dv_{nuc} v_{m,nuc}} \tag{34}$$

where $v_{m,nuc}$ is the representative volume (midpoint) in the section that covers the volume of nuclei and dv_{nuc} is the interval of that section, respectively. The coefficient a_{nuc} in Eq. 32 takes the form:

$$a_{nuc} = 2 \frac{w_{nuc}}{[\mathrm{dimer}]^2} \tag{35}$$

where the factor 2 indicates the fact that two dimers are consumed to form a soot nucleus.

When a dimer collides with a large soot particle, the two PAH molecules will deposit on the surface [55]. Within a section i, the change in the number density due to condensation is classified into three types: a) condensation of dimers on particles of section i, $\omega_{cond,dimer\to i}$, b) condensation of dimers on particles of section $i-1$ that will enter into section i, $\omega_{cond,i-1\to i}$, and c) condensation of dimers on particles of section

i that will go to section $i+1$, $\omega_{cond,i\to i+1}$. These contributions will be included via a condensation source term $C(v,\mathbf{Y})$ into Eq. 3 in a manner ensuring that the total volume added by condensation is conserved. The impact on the primary particle number density is addressed later in this section. The condensation rate for each of the aforementioned types is evaluated as follows [25]:

$$\omega_{cond,\mathrm{dimer}\to i} = [\mathrm{dimer}]N_\mathrm{A}\int_{v_{i-1}}^{v_i-v_\mathrm{dimer}} \beta_{d,i}N(w)dw \quad = [\mathrm{dimer}]N_\mathrm{A}\beta_{d,i}(dv_i - v_\mathrm{dimer})N_i \tag{36}$$

$$\omega_{cond,i-1\to i} = [\mathrm{dimer}]N_\mathrm{A}\int_{v_{i-1}-v_\mathrm{dimer}}^{v_{i-1}} \beta_{d,i-1}N(w)dw = [\mathrm{dimer}]N_\mathrm{A}\beta_{d,i-1}v_\mathrm{dimer}N_{i-1} \tag{37}$$

$$\omega_{cond,i\to i+1} = [\mathrm{dimer}]N_\mathrm{A}\int_{v_i-v_\mathrm{dimer}}^{v_i} \beta_{d,i}N(w)dw \quad = [\mathrm{dimer}]N_\mathrm{A}\beta_{d,i}v_\mathrm{dimer}N_i \tag{38}$$

where the collision frequency of a dimer and a soot particle in the section (v_{i-1}, v_i) is calculated as follows:

$$\beta_{d,i} = 1.3\sqrt{\frac{\pi k_\mathrm{B}T}{2\rho_s}}\left(d_\mathrm{dimer}+d_{g,i}\right)^2\sqrt{\frac{1}{v_\mathrm{dimer}}+\frac{1}{v_{m,i}}} \tag{39}$$

where $v_{m,i}$ is the volume at the middle of the section, the collision diameter of the particle $d_{g,i}$ at section i is evaluated according to Eqs. 4 and 5, and the amplification factor of 1.3 is due to Van der Waals interactions [58]. Therefore, the coefficient b_{cond} in Eq. 32 is determined as:

$$b_{cond} = \frac{\sum\left(\omega_{cond,\mathrm{dimer}\to i}+\omega_{cond,i-1\to i}-\omega_{cond,i\to i+1}\right)}{[\mathrm{dimer}]} \tag{40}$$

where special treatment is applied for the first volume section to cancel type 2 condensation $\omega_{cond,i-1\to i}$. With the help of Eq. 35 and Eq. 40, one solves the quadratic equation Eq. 32 to obtain the concentration of dimers. Now the condensation source term $C_i(v,\mathbf{Y})$ for the number density of aggregates in the section (v_{i-1}, v_i) can be evaluated as:

$$C_i(v,\mathbf{Y}) = \left(\omega_{cond,\mathrm{dimer}\to i}+\omega_{cond,i-1\to i}-\omega_{cond,i\to i+1}\right)\frac{v_\mathrm{dimer}}{v_{m,i}dv_i} \tag{41}$$

We now formulate the condensation source term for primary particles as follows:

$$C_{p,i}(v,\mathbf{Y}) = \left(\omega_{cond,\mathrm{dimer}\to i}n_{av,i}+\omega_{cond,i-1\to i}n_{av,i-1}-\omega_{cond,i\to i+1}n_{av,i}\right)\frac{v_\mathrm{dimer}}{v_{m,i}dv_i} \tag{42}$$

5.3. Surface growth and oxidation

Soot surface growth and oxidation are modelled via the H-abstraction/C_2H_2 addition (HACA) mechanism, originally proposed by Frenklach and Wang [59]. The reaction rates are calculated based on the parameters of Tables 2 and 3 in Ref. [55]. The theoretical maximum value of the overall site density, χ_soot, has been estimated to be 2.3×10^{19} sites/m^2 [59]. The concept of surface reactivity was introduced in the HACA mechanism in the form of a parameter, α, and the main uncertainty in HACA lies in the determination of this parameter. Constant values were employed in early research [59], but later work considered it to be a function of the local temperature [60] and other parameters, such as particle size [61]. Recent

studies [36, 37] proposed a more complex model that accommodates the effects of both temperature and residence time. As the focus of this study is on the investigation of the CFV-2PBE method, a simple model for α was adopted, in which α is a function of temperature only, assuming the form $\alpha = \mathrm{a}\cdot\exp(9000/T)$ [60]. The pre-exponential factor, a, was adjusted such that the peak value for integrated soot volume fraction is matched to a satisfactory degree with the experimental data (Sec. 7.2). The net growth rate (including oxidation) is calculated as follows:

$$G(v, \mathbf{Y}) = \frac{a(v)}{\rho_s} R_g(\mathrm{HACA}) \tag{43}$$

where $a(v)$ denotes the soot surface area and $R_g(\mathrm{HACA})$ is the mass growth rate, which is a function of α, χ_{soot}, reaction rates and the local concentrations of species associated with the HACA mechanism [55, 59].

5.4. Aggregation

The collision kernel β takes different forms depending on the Knudsen number, $\mathrm{Kn} = 2\lambda_f/d$, where λ_f is the gas mean free path and d is the particle diameter. Three regimes can be identified, namely the free molecule regime ($\mathrm{Kn} < 0.1$), continuum regime $\mathrm{Kn} > 10$ and transition regime ($0.1 < \mathrm{Kn} < 10$). The equations are [62, 63]:

$$\begin{aligned}
\beta^{fm}(v_i, v_j) =& E_F \sqrt{\frac{\pi k_{\mathrm{B}} T}{2\rho_s}} \left(\frac{1}{v_i} + \frac{1}{v_j}\right)^{1/2} \left(d(v_i) + d(v_j)\right)^2 \\
\beta^{c}(v_i, v_j) =& \frac{2k_{\mathrm{B}} T}{3\mu} \left(\frac{\mathrm{Cu}(v_i)}{d(v_i)} + \frac{\mathrm{Cu}(v_j)}{d(v_j)}\right) \left(d(v_i) + d(v_j)\right) \\
\beta^{t}(v_i, v_j) =& \frac{\beta^{fm}(v_i, v_j)\beta^{c}(v_i, v_j)}{\beta^{fm}(v_i, v_j) + \beta^{c}(v_i, v_j)}
\end{aligned} \tag{44}$$

where $\mathrm{Cu}(v_i) = 1 + 1.257\mathrm{Kn}_{v_i}$ is the Cunningham slip correction factor and $d(v)$ represents either the spherical particle diameter or the collision diameter of an aggregate that can be evaluated from Eq. 5. In the present work, the fractal dimension and fractal prefactor for all aggregates are taken to be $D_f = 1.8$ [44, 46, 48] and $k_f = 1.94$ [47], respectively.

5.5. Fusing of soot primary particles

The term 'sintering' is usually employed in material science and also in the study of inorganic nanoparticles such as silica and titania to denote the fusing of primary particles. However, as recently discussed by Michelsen et al. [22], this terminology may be inappropriate for soot, where the physical mechanisms are different. In accordance with that recommendation, in the present paper the term 'coalescence' refers to the formation of spherical particles as a result of collisions between incipient particles (i.e. formation of particles below the cut-off point in the two-PBE model), while the merging of primary particles within aggregates will be referred to generally as fusing. The term 'sintering' is retained in this study when referring to inorganic nanoparticles.

Table 1: Summary of parameters in the sintering models and their units

Variable	Silica particle model	Titania particle model
	Range given in Ref. [40] (units)	Value given in Refs. [29, 65] (units)
A_s	1.1×10^{-14} (s/m)	7.44×10^{16} $\left(\mathrm{s}/\left(\mathrm{K}\cdot\mathrm{m}^4\right)\right)$
E_a	$1.8 \times 10^4 \leqslant E_a \leqslant 1.8 \times 10^5$ (K)	3.31×10^4 (K)
d_c	$1 \leqslant d_c \leqslant 5$ (nm)	-

The characteristic timescale of fusing plays an important role in shaping the structure of an aggregate. The sintering behaviour of several nanoparticles has been studied in the aerosol community but, to our knowledge, such information is not available on soot. As a result, the few studies that have attempted to incorporate a model with for a finite rate of fusing of soot primary particles have been based on extrapolation from sintering models for different nanoparticles. In a study of laminar premixed ethylene sooting flames, Chen et al. [40] employed the expression of τ_s for silica particles [64]:

$$\tau_s = A_s d_{p,i} \exp\left[\frac{E_a}{T}\left(1 - \frac{d_c}{d_{p,i}}\right)\right] \tag{45}$$

where A_s, d_i and E_a are the pre-exponential factor, the diameter of the sintering primary particle and the activation energy, respectively. On the other hand, Veshkini et al. [39] employed an expression for the sintering of titanium oxide [65] in the Santoro laminar ethylene diffusion flame:

$$\tau_s = A_s d_{p,i}^4 T \exp\frac{E_a}{T} \tag{46}$$

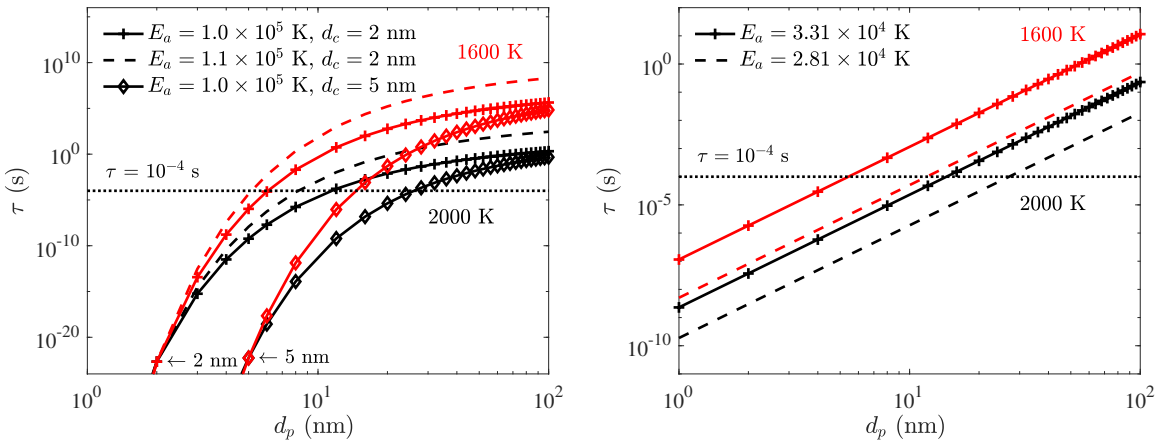
The coalescence between two spherical particles in contact is a result of various molecular transport mechanisms in the contact region [42]. For liquid particles, such as silica, sintering is driven by viscous flow. On the other hand, transport by diffusion is the dominant route for the sintering of crystalline titania nanoparticles in contact. Even in the context of SiO_2, as indicated in a recent work by Goudeli et al. [66], different sintering models show distinct differences in the predicted primary particle diameter and collision diameter. The predicted fusing behaviour of soot particles could be significantly different depending on the sintering model employed, and transposing these kinetics to soot inevitably brings uncertainties into soot modelling. As the current information on the fusing of soot primary particles is not sufficient to reach consensus, in the current study models for both silica and titania will be applied and tested, and their impact on the model outcome will be investigated via a parametric analysis. As a base case for adopting the sintering model of silica particles, a set of optimised parameters from the work of Chen et al. [40] is employed, while for the titania model we adopt the data of Refs. [29, 65], also applied in Ref. [39]. A detailed summary can be found in Table 1.

Before applying the models to the flame, we conduct here a sensitivity analysis of the parameters in both sintering models to provide guidance for their use in the sooting flame simulation. In Fig. 2 we show, for each

model, the sintering timescale at two thermal conditions that are typical of the regions of centreline (1600 K) and the flame front (2000 K) in the forthcoming application to the flame. Since varying the pre-exponential factor A_s in both models only causes a vertical movement of the curve, the impact of this parameter is not shown. The dotted line represents an effective sintering timescale, above which the sintering is nearly ceased. It can be seen that the temperature has a profound impact on the sintering rates for both models. At a certain temperature, the characteristic sintering timescale reaches an asymptote with increasing primary particle diameter d_p in silica model. The position of this asymptote is affected by E_a. When employing the silica model, therefore, one needs to adjust both parameters with caution. On the other hand, there is only one parameter to be adjusted in the titania model. Moreover, the sintering rate is relatively large for small particles in titania model, justifying our approach of assuming sintering to be instantaneous for particles less than d_c (Sec. 4.1). In the following applications, the value of critical diameter d_c in the titania model is set to be 3 nm. Below that value, the results show little sensitivity to d_c.

6. Validation of the CFV-2PBE method: self-preserving distribution of aggregates

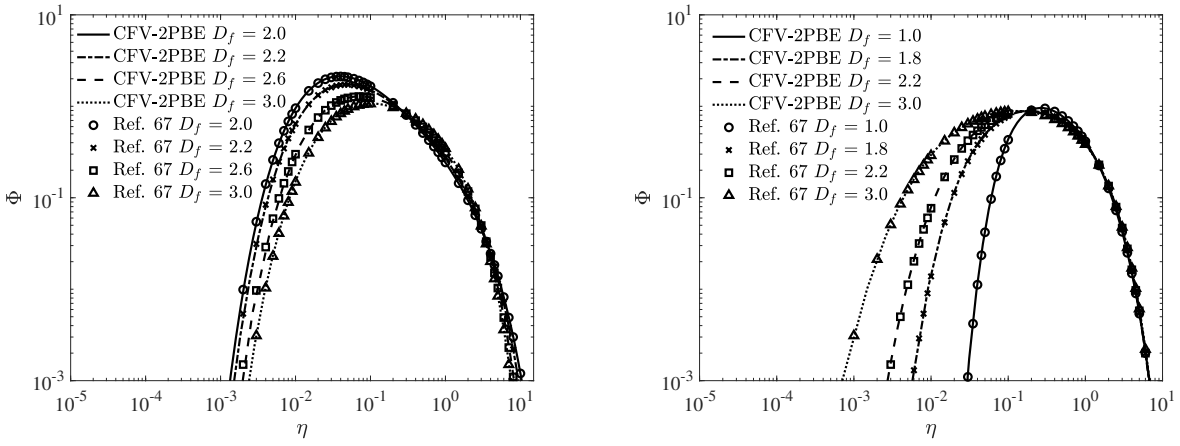
Prior to be employed in the flame, the CFV-2PBE method will first be validated by computing the self-preserving distribution of aggregates and comparing it to the study of Vemury and Pratsinis [67]. In these calculations, it is assumed that the primary particle size remains the same, and the particle growth is only by aggregation in both the free molecule and continuum regimes. The expressions for the collision frequencies β are the same as in Eqs. 4 and 6 in Ref. [67]. In all computations, the number density of the initially monodisperse particles is $N_0 = 1 \times 10^{13}$ m^{-3}, the initial particle size is $v_{p_0} = 1 \times 10^{-27}$ m^3 and the



(a) Silica model (b) Titania model

Figure 2: The impact of varying each model parameter on the characteristic sintering time for (a) the silica model, (b) the titania model. The characteristic time τ is plotted as a function of primary diameter for two different temperatures. The sintering timescale at 1600 K is marked with red colour, while the sintering timescale at 2000 K is marked with black colour.

fractal prefactor (Eq. 5) is $k_f = 1$. The particle density is that of soot particles and the temperature is set to $T = 1700$ K. The dimensionless particle volume is $\eta = Nv/V$ and the dimensionless particle number density function is $\Phi = Vn/N^2$, where V and N are the total particle volume fraction and number concentration respectively [68]. For a given D_f, the self-preserving distribution is attained when the distribution in the (η, Φ) coordinates does not change any more with time. In the first calculation, all the particles are assumed to be aggregates (by setting the critical diameter d_c smaller than the volume-equivalent diameter of the first volume section) and no sintering is considered. Fig. 3 shows the self-preserving distribution of aggregates in the free molecule and continuum regime for several values of D_f, while Fig. 4 shows the geometric standard deviation as a function of D_f. In all cases, the results are in excellent agreement with those of Vemury and Pratsinis [67].

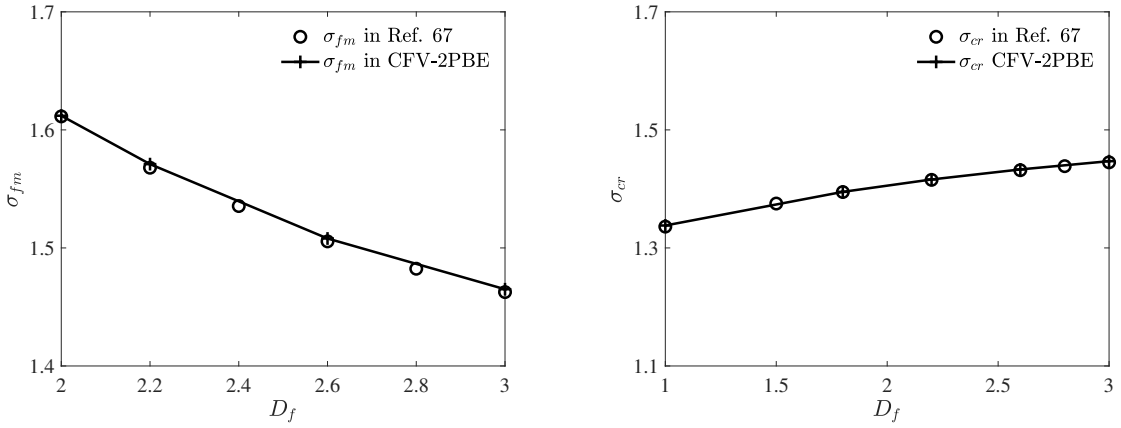


(a) Free molecule regime

(b) Continuum regime

Figure 3: Self-preserving distribution of aggregates with varying D_f in the free molecule and continuum regimes by the CFV-2PBE method, comparison with the results by Vemury and Pratsinis [67].

The impact of sintering is now introduced by employing different sintering rates over the entire size range. Fig. 5 shows the self-preserving distribution of aggregates with $D_f = 2.0$ in the free molecule regime, with the sintering rate increasing from zero (Case 4) to instantaneous sintering (Case 1). Case 4 yields the same self-preserving distribution as that of $D_f = 2.0$, while instantaneous sintering yields the self-preserving distribution for spherical particles. When a finite sintering rate is employed, self-preserving distributions with intermediate shapes are obtained. A similar pattern is observed for both free molecule and continuum regimes, and therefore only the case for $D_f = 2.0$ in the free molecule regime is shown.



(a) Free molecule regime (b) Continuum regime

Figure 4: Geometric standard deviation of the self-preserving distribution of aggregates as a function of D_f in the free molecule and continuum regimes, comparison with the results by Vemury and Pratsinis [67].

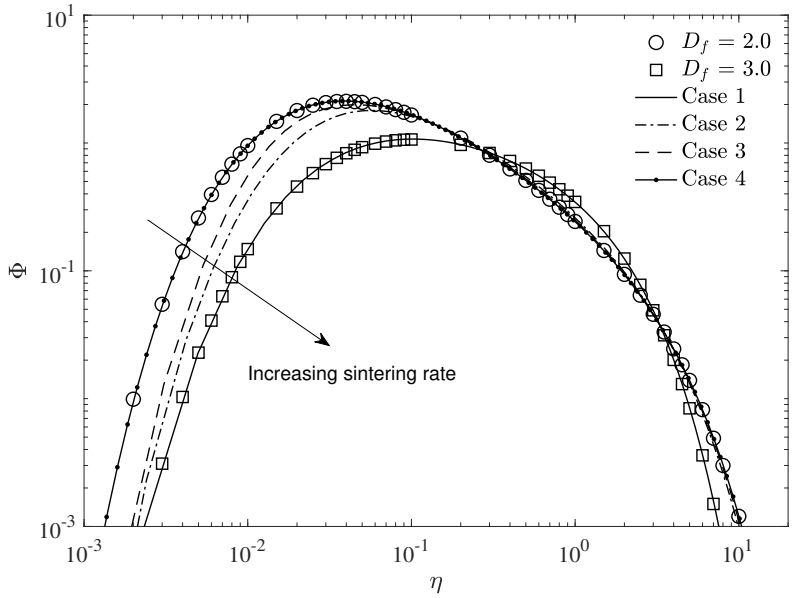


Figure 5: Self-preserving distribution of aggregates having $D_f = 2.0$ in free molecule regime under different sintering rates. The dots and the squares represent the results by Vemury and Pratsinis [67] for $D_f = 2.0$ and spherical particles, respectively. The sintering rate increases from zero (Case 4) to instantaneous sintering (Case 1)

7. Simulation of a laminar non-premixed co-flow sooting flame

7.1. Flame configuration and numerical setup

The target flame in our study is the non-smoking ethylene-air diffusion flame at atmospheric pressure investigated by Santoro et al. [41, 69]. This flame was chosen due to the availability of experimental data [45, 70, 71] and the fact that it has been the subject of several modelling studies (Refs. [20, 35, 39, 72] among others). Furthermore, unlike flames that can be simulated via one-dimensional formulations, this flame requires full coupling with a CFD code, and is thus an intermediate stage before applying the CFV-2PBE method to turbulent flames. The flame consists of a central fuel jet (pure ethylene) of diameter 11.1 mm surrounded by a concentric air co-flow of diameter 101.6 mm at atmospheric pressure and temperature. The inlet flow rates for the fuel and air are 3.85 cm^3/s and 713.3 cm^3/s, equivalent to velocities of 3.98 cm/s and 8.9 cm/s, respectively. An illustration of the burner is shown in Fig. 6.

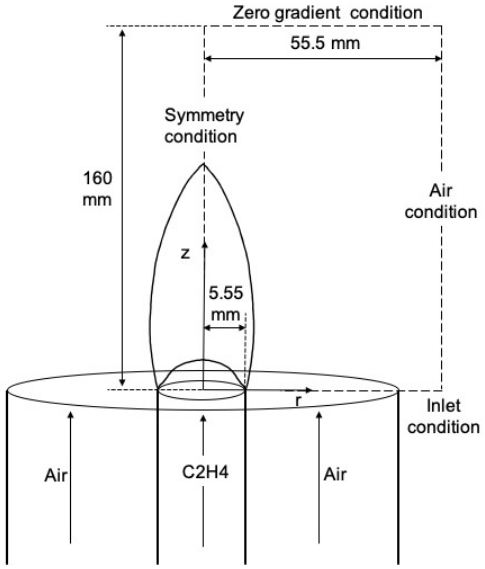


Figure 6: Illustration of the burner and the computational domain.

The computational domain is cylindrical in shape and spans 160 mm in the axial direction with 200 cells and 55.5 mm in the radial direction with 100 cells (Fig. 6). The grid is stretched axially and radially by factors of 1.01 and 1.03, respectively. A convergence study showed that further refinement of the grid was not needed. There is an uncertainty regarding the inlet condition, as some amount of heat is transferred from the flame base to the burner nozzle, thus altering the inlet temperature and velocity profiles. According to Guo et al. [73], the prediction can be improved quantitatively with an increase in fuel temperature, and such a strategy has been adopted in several studies [35, 39] where the amount of preheating was chosen so as to obtain the best match of the results with the experimental data. Since our interest lies in the study of the two-PBE model and the CFV-2PBE method, rather than in obtaining the best possible match with

experimental data, it was decided to keep adjustments to a minimum, and therefore uniform velocity profiles for fuel at 300 K and for air at 300 K have been employed. Regarding the discretisation of the PBE, we employ a geometric grid with 60 intervals in the volume domain corresponding to particle sizes from 0.72 nm to 1240 nm, and again grid convergence was tested via successive refinements.

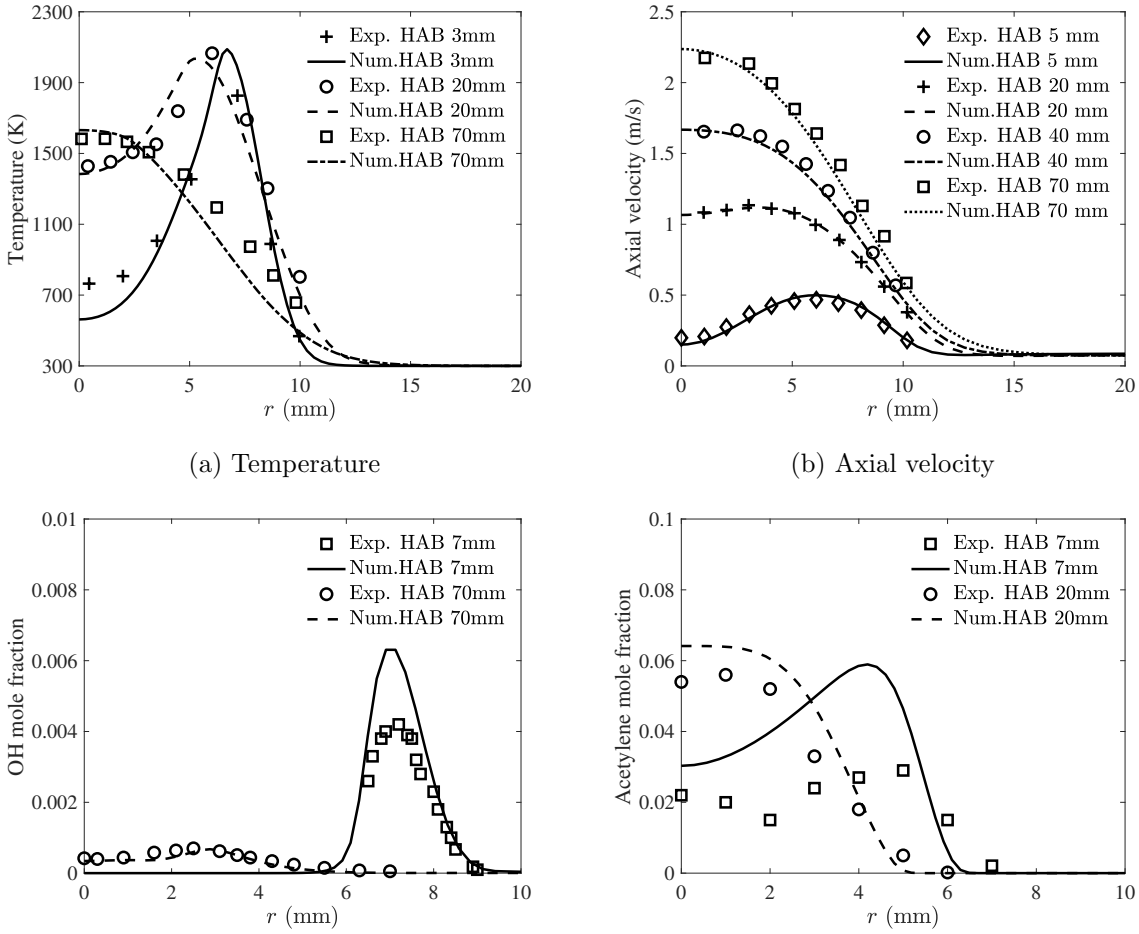
7.2. Overall validation

In the following sections, we are going to present the simulation results from both the CFV-1PBE and CFV-2PBE methods in the following order. Comparisons of temperature, axial velocity, concentration and integrated soot volume fraction at different heights above burner (HAB) are presented first, followed by an investigation of soot morphology along the flame centreline and the pathline of maximum soot volume fraction at each axial location. Afterwards, a detailed parametric study of the key parameters in both the CFV-1PBE and CFV-2PBE models will be conducted. The data available related to soot morphology are summarised in Table 2. At each spatial location, a geometric average [74] is applied over the volume-equivalent diameter ranging from 1.5 nm to 1024 nm to provide a good measure of particle size. Note that, for the base case of CFV-1PBE, the cut-off point $d_c = 30.8$ nm, a value that has also been adopted in a recent work of Liu et al. [26], while the sintering model parameters for the base case of CFV-2PBE are $d_c = 5$ nm, $E_a = 10.0 \times 10^4$ K for the silica model and $E_a = 3.31 \times 10^4$ K for the titania model. For the parameter A_s, one may refer to Table 1.

Table 2: Summary of experimental data on soot aggregates in the flame investigated in this study and their sources

Soot data	Spatial position		Unit
	Centreline	Pathline having maximum soot f_v	
f_v	[41, 69]	[41, 69]	ppm
d_p	-	[70, 71]	nm
N	-	[69]	m^{-3}
N_p	-	[71]	m^{-3}
n_{av}	-	[71]	-

The numerical results from both CFV-1PBE and CFV-2PBE (with both sintering models) are both in good agreement with experiments regarding the radial distributions of temperature, axial velocity, OH and C_2H_2 at different HAB, and therefore only the results generated from the CFV-1PBE method are shown. Fig. 7a shows the temperature profiles at three different HAB, and the overall shapes and trends of the experimental profiles are well represented. At 3 mm HAB, there is a slight underprediction between $r = 0.0$ mm and $r = 4.0$ mm, most likely due to the effect of preheating. The profiles of axial velocity are also reproduced very well, as shown in Fig. 7b. Predicted and measured OH mole fraction profiles are compared in Fig. 7c. The simulated profile captures the peak position of OH profiles at both HAB, yet with a considerable overprediction for peak values at 7 mm HAB. It should be noted that the experimental



(a) Temperature

(b) Axial velocity

(c) Mole fraction of OH

(d) Mole fraction of C_2H_2

Figure 7: Comparison of numerical predictions and experimental data in radial direction for (a) temperature (measurements from Ref. [69]), (b) axial velocity (measurements from Ref. [69]), (c) OH mole fraction (measurements from Ref. [69]), and (d) acetylene mole fraction (measurements from Ref. [75]). Only results from CFV-1PBE are shown, as the other models have a similar performance.

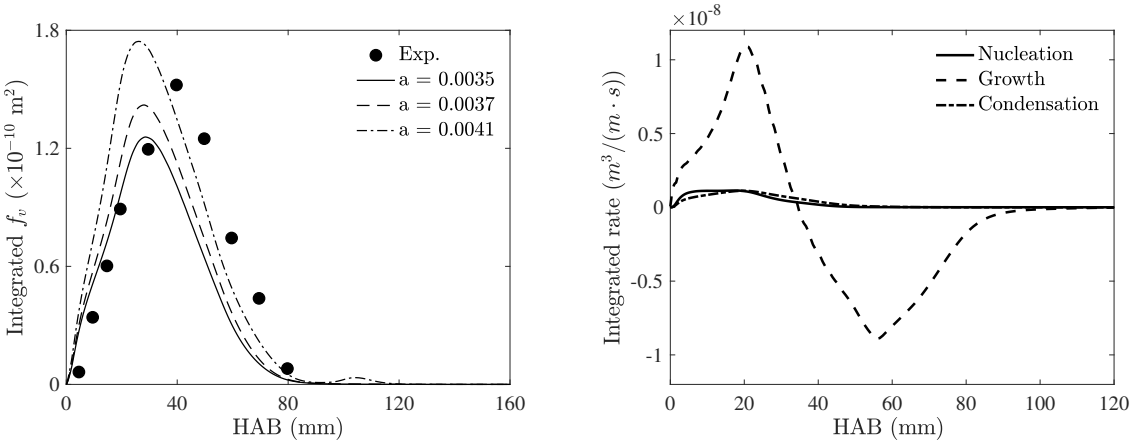
errors for OH measurement with laser-induced fluorescence (LIF) could be as much as 50% [75], hence the agreement is reasonable. Fig. 7d shows the acetylene mole fraction profile at 7 mm and 20 mm HAB. The general shape of the curves at both axial locations is well captured, despite some overprediction at the lower region of the flame. A similar level of overprediction can be found in the work by Zhang et al. [43], Veshkini et al. [36], and Akridis and Rigopoulos [76] and, again, a likely cause is fuel preheating. It is worth noting that, while most of the soot mass is added via acetylene addition, the rate-limiting reactions in the current HACA mechanism are the hydrogen abstraction reactions (the forward reactions of No.1 and No.2 in Ref. [55]). Therefore, an accurate prediction of H and, to some extent, OH radicals (which also contribute to oxidation) is more important for surface growth than C_2H_2 [36]. Overall, satisfactory agreement is achieved for the prediction of the thermal and chemical environments that are important in soot prediction.

We now examine the integrated soot volume fraction at different HAB, for which experimental data are available. This variable is likely to be dominated by surface reactions, which play a major role in soot mass growth, as has been confirmed by several studies [36, 41, 69, 77, 78]. However, as discussed in Ref. [78], our knowledge of the surface reactivity of soot is rather limited. The common site density $\chi = 2.3 \times 10^{19}$ sites/m^2 reported by Frenklach and Wang [59] is viewed as a theoretical limit, and no exact value of χ is currently available [78]. Fig. 8a compares the calculated and measured distributions of the integrated soot volume fraction along the flame axis for different values of the prefactor a in the expression for the surface reactivity. With increasing surface reactivity, the peak value of the integrated soot volume fraction experiences a significant increase. Fig. 8b shows that HACA surface growth is the dominant mechanism for the soot generation and that the position of the peak value for the profile of the integrated soot volume fraction coincides with the one in surface growth phenomena. As our intention is to investigate the impact of aggregation models, the pre-exponential factor in the surface reactivity expression was adjusted so that the peak value of the integrated soot volume fraction from the simulation is close to that of the experiment, while the values of all the other parameters of the soot model were adopted from the literature without modification. In the following analysis, therefore, the surface reactivity is yielded by the expression $\alpha = 0.0037 \times e^{9000/T}$.

Fig. 9 shows the calculated integrated soot volume fraction for the base case of the CFV-1PBE and CFV-2PBE methods. It can be seen that the soot yield in the CFV-2PBE method is similar to that of the CFV-1PBE method. It must also be noted that, with the current chemical mechanism and soot model, the entire profile appears to be somewhat shifted towards the fuel nozzle, a fact that was also observed in Ref. [55].

7.3. Centreline comparisons

In the present section, the numerical results predicted by the CFV-1PBE method and CFV-2PBE method with the two sintering models discussed in Sec. 5.5 are presented. Fig. 10 shows comparisons of the soot



(a) Integrated soot volume fraction (b) Integrated rate for each processes

Figure 8: (a) Integrated soot volume fraction along the axial direction for different values of the prefactor a in the expression for the surface reactivity with the CFV-1PBE method (line: calculation, symbol: measurements [69]), and (b) breakdown of the integrated soot volume fraction rate of change due to nucleation, HACA surface reactions and condensation for the case of prefactor a = 0.0037.

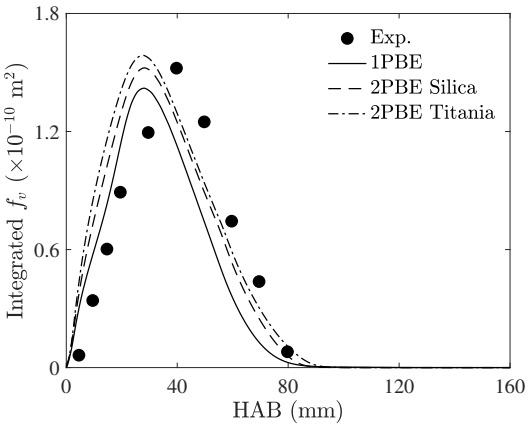
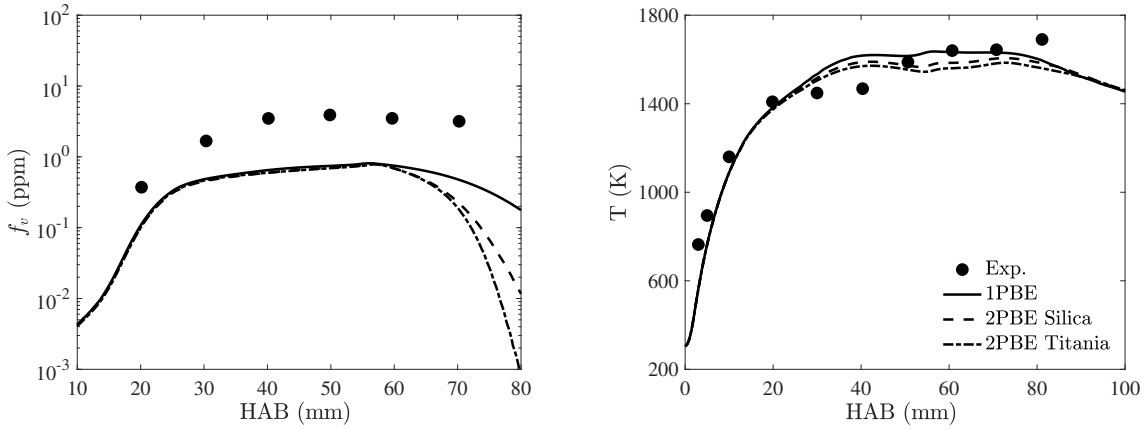


Figure 9: Comparison of the numerical predictions and experimental data for the integrated soot volume fraction along the axial direction from the base case of the CFV-1PBE method and CFV-2PBE method.

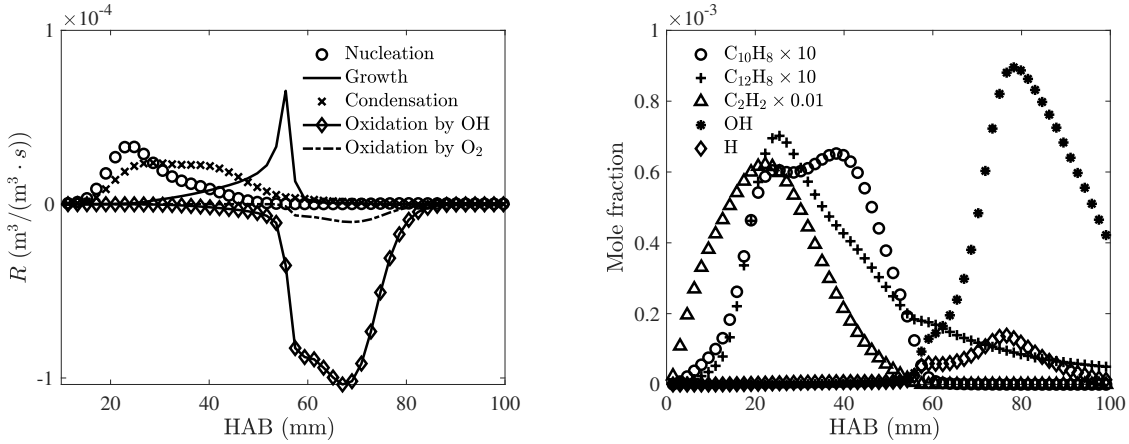
volume fraction and temperature along the centreline with the experimental results. All three models give similar results and underpredict the soot volume fraction by an order of magnitude, while the temperature predictions are in good agreement with the measurements. A possible cause of this discrepancy is the uncertainty involved in the experimental measurements. The soot volume fraction measurements by Santoro et al. [41, 69] employed the laser extinction/scattering approach with a constant refractive index (RI) without taking into account the soot composition and morphology which, as indicated in a recent work by Kelesidis and Pratsinis [79], might lead to an overestimation of soot volume fraction by as much as 100%. The underprediction of the soot along the flame centreline has also been observed in the work of Dworkin et al. [35]. Another possible cause could be the soot kinetics. To probe further into this, a breakdown of the source terms contributing to soot volume fraction (nucleation, HACA surface growth, condensation, oxidation by OH and O_2) is shown in Fig. 11a. Between HAB 20 mm and 45 mm, nucleation and condensation are the dominant mechanisms. Although a rapid increase for soot surface growth can be seen after HAB 55 mm, this impact is soon cancelled by oxidation due to OH radicals. In the current soot kinetics, nucleation and condensation depend on the dimer concentration, which is highly sensitive to the concentration of PAHs. Fig. 11b shows the dominant PAHs (i.e. those whose mole fraction is greater than that of other PAHs by an order of magnitude). The formation of small PAHs occurs at the first stage of the flame (from HAB = 5 mm to HAB = 20 mm), after which the temperature is stabilised and the PAHs are gradually consumed. The formation of OH and H starts approximately at HAB = 50 mm. Subsequently, the OH and H radicals trigger the H-abstraction in the HACA mechanism, boosting the surface growth rate for a short distance. The shape of the growth profile is due to the low concentration of C_2H_2 when reaching HAB 60 mm, thus limiting the acetylene addition. In the meantime, the oxidation by OH counters the increase due to surface growth. Other studies [35, 36] have also found that the soot mass addition along the centreline is mainly through nucleation and condensation. This feature explains why CFV-2PBE provides similar results as CFV-1PBE. One of the major advantages of CFV-2PBE is the better prediction of particle surface area (to be discussed in Sec. 7.4), which plays a dominant role only in the surface growth and oxidation processes. Therefore, this underprediction is not related to the aggregation model.

In Fig. 12, the particle size distribution (PSD) of soot aggregates is shown at three locations along the centreline. Due to the lack of experimental data for the PSD, no such comparison can be made. It is notable, however, that the predictions of the three models differ considerably, in spite of the total soot volume fraction being similar. In the nucleation region, most of the particles are newly formed and exhibit a unimodal PSD, and the differences between the three models are small. In the growth region, where both growth and aggregation are present, bimodal PSDs are predicted by the CFV-2PBE model with the sintering models, very different from the CFV-1PBE prediction. This feature illustrates the strong impact of primary particle size on the PSD, an observation consistent with the findings of a recent study by Bouaniche et al. [3], where the impact of primary particle size on the PSD was investigated in a premixed flame using a



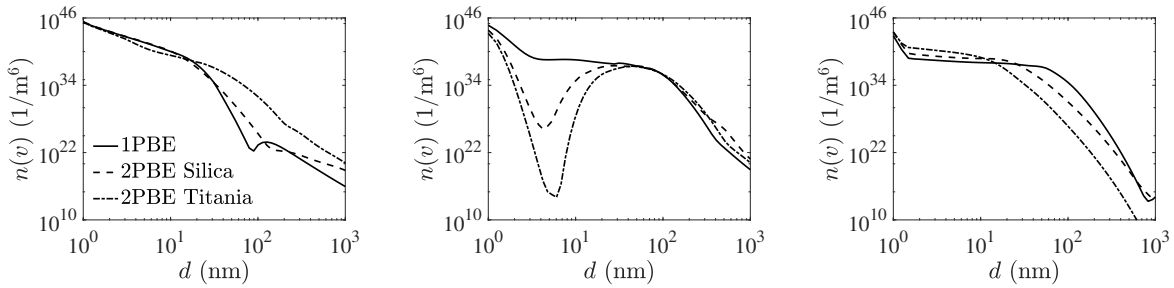
(a) Soot volume fraction (b) Temperature

Figure 10: Comparison of numerical predictions by CFV-1PBE and CFV-2PBE with two sintering models with experimental data along the centreline for (a) soot volume fraction (measurements from Refs. [41, 69]), (b) temperature (measurements from Refs. [45, 69])



(a) Contribution rates R for soot volume fraction (b) Species mole fraction

Figure 11: The rates of change for each soot formation process and the predicted species mole fractions along the centreline by the CFV-1PBE method



(a) 15 mm HAB (b) 50 mm HAB (c) 80 mm HAB

Figure 12: Comparison of the numerical predictions of soot aggregate number density distribution by CFV-1PBE and CFV-2PBE of two sintering models at three probe locations along the centreline: (a) 15 mm HAB (nucleation region), (b) 50 mm HAB (growth region), and (c) 80 mm HAB (oxidation region)

hybrid stochastic/fixed-sectional method. When soot enters the oxidation zone, the PSD becomes unimodal again.

7.4. Comparisons with results along pathline of maximum soot volume fraction

In the present section, the results of both PBE models are compared with the experimental results along the soot particle path exhibiting maximum soot volume fraction. Moreover, the effect of the key parameters in both modelling approaches (one-PBE and two-PBE) are analysed in order to assess the effect of modelling uncertainties. The discussion will focus on the parameters related to aggregation, rather than on parameters that are implemented in the same way in both the CFV-1PBE and CFV-2PBE models, such as the surface reactivity.

Firstly, we investigate the impact of the artificial cut-off point that controls the morphology of soot in the CFV-1PBE model. In Fig. 13, we compare the results from CFV-1PBE with $d_c = 30.8$ nm and $d_c = 20$ nm along the maximum soot pathline where intense growth and high temperatures are expected. A smaller cut-off point would, in principle, lead to a larger number of primary particles within an aggregate, and this is indeed the case, as shown in Figs. 13b,c. Also, as indicated in Figs. 13e,f, a larger surface area given by the case of $d_c = 20$ nm would enhance soot surface growth, leading to a larger soot yield. As expected from the construction of the one-PBE model, the average diameter of primary particles in both cases grows up to the size of the cut-off point and afterwards remains constant (see Fig. 13d). The difference in the total number density is significant in the initial region, as shown in Fig. 13a. In practice, one needs to choose the cut-off size d_c with care in order to achieve a good prediction of both soot volume fraction and soot morphology.

For the CFV-2PBE model, the need is shifted to the determination of the rate of fusion for the primary particles, which shapes the structure of soot aggregates. Therefore, we investigate the impact of the key parameters in the two sintering models employed in the framework of CFV-2PBE. For the silica model,

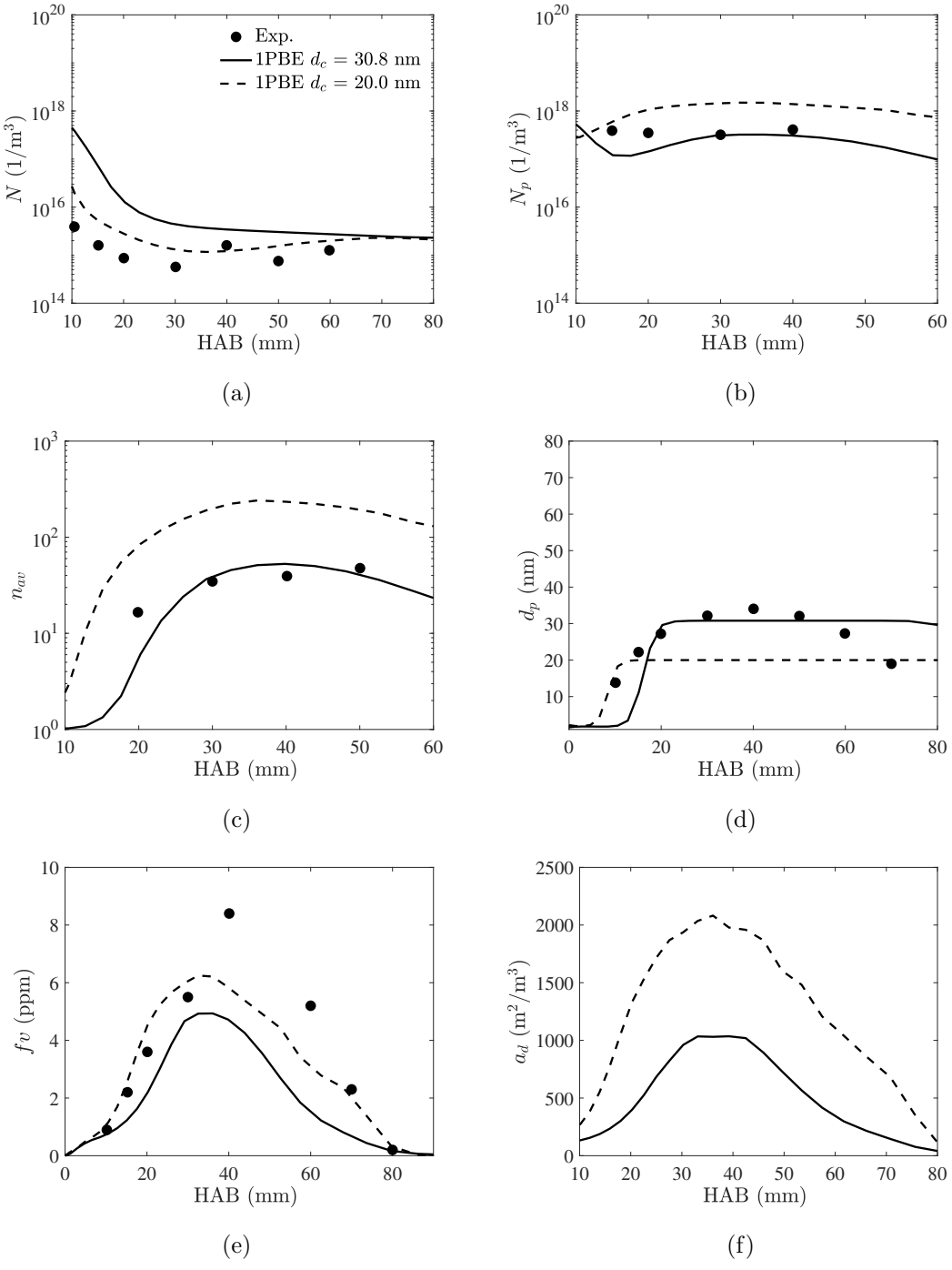


Figure 13: Comparison of CFV-1PBE model predictions along the annular pathline containing maximum soot volume fraction with experimental data, and effect of cut-off point. (a) Number density of aggregates, (b) number density of primary particles, (c) average number of primary particles per aggregate, (d) diameter of primary particles, (e) soot volume fraction, and (f) surface area density. Solid line: CFV-1PBE with $d_c = 30.8$ nm; dashed line: CFV-1PBE with $d_c = 20.0$ nm

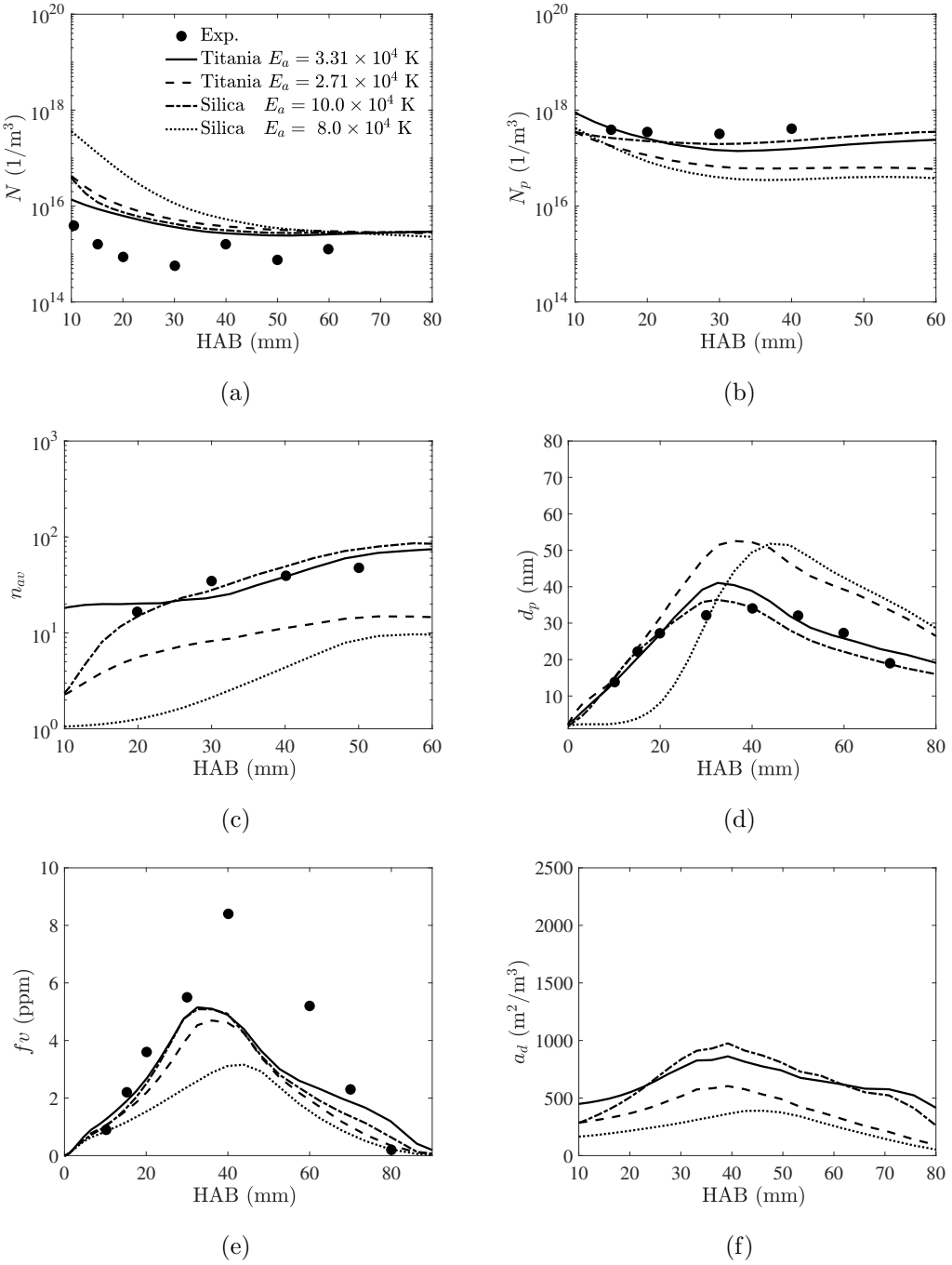


Figure 14: Comparison of CFV-2PBE model predictions along the annular pathline containing maximum soot volume fraction with experimental data, and effect of different activation energies with the silica and titania model. (a) Number density of aggregates, (b) number density of primary particles, (c) average number of primary particles per aggregate, (d) diameter of primary particles, (e) soot volume fraction, and (f) surface area density. Solid line: titania model with $E_a = 3.31 \times 10^4$ K; Dashed line: titania model with $E_a = 2.71 \times 10^4$ K; Dash-dot line: silica model with $d_c = 5$ nm, $E_a = 8.0 \times 10^4$ K; Dotted line: silica model with $d_c = 5$ nm, $E_a = 10.0 \times 10^4$ K.

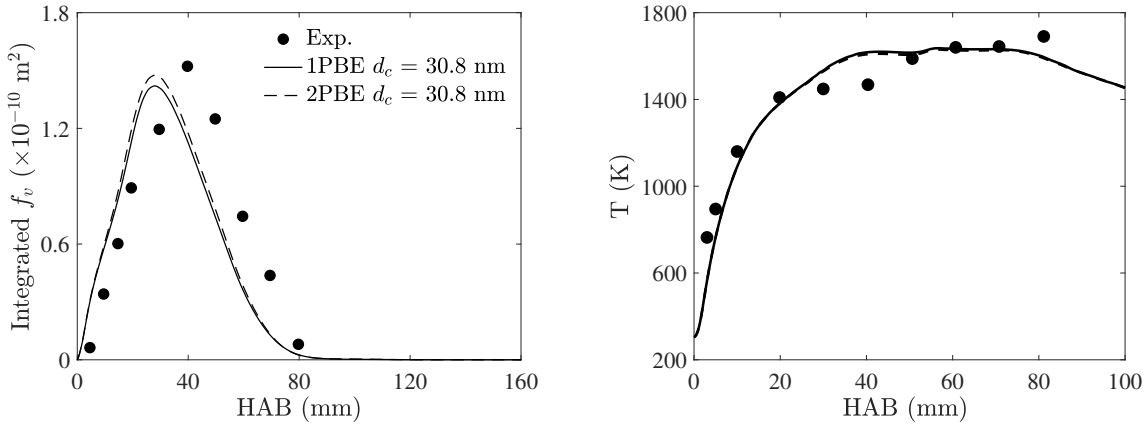
cases having critical diameter $d_c = 5$ nm with different activation energy are investigated, while for the titania model there is only the activation energy to vary. For the titania model, soot aggregates tend to form earlier in the case of slow sintering rate, the aggregate number density is smaller and the number of primary particles is higher (Fig. 14a,b). The slow sintering rate also leads to a greater number of primary particles and a larger surface area, and thus larger soot volume fraction, as indicated in Figs. 14c,e,f. A similar pattern can be seen in the silica model. Overall, a high sintering rate in either model would result in larger primary particles. Consequently, the model behaviour shares a similar pattern with the case of a large cut-off point in the CFV-1PBE method, except for the prediction of the average diameter of primary particles. Fig. 14d shows that there is a significant difference in the predicted primary particle size with different sintering parameters, which is in accordance with the study of Goudeli et al. [66].

7.5. Comparison of the one-PBE model with the two-PBE model without finite-rate fusing of primary particles

Finally, it is worth comparing the results of the CFV-1PBE with those of a CFV-2PBE formulation that does not involve finite-rate fusing of primary particles and employs the same critical diameter ($d_c = 30.8$ nm) as the CFV-1PBE model. This comparison exposes the influence of the inconsistent calculation of surface growth and oxidation in the one-PBE formulation, which (as discussed in Sec.1) is due to the fact that the size of the primary particles is assumed to be frozen once they reach the cut-off size, ignoring the effect of surface processes. Fig. 15 shows the comparison of integrated soot volume fraction and temperature along the centreline, while Fig. 16 shows the comparison along the annular pathline containing maximum soot volume fraction for the average number of primary particles per aggregate and the diameter of primary particles. Small differences can be observed in both figures, and a similar trend is observed in other plots (not shown here). The impact of the inconsistent calculation of surface processes is therefore small, due to the fact that the effect of these processes on the particle properties beyond such a high cut-off point is small. Of course, the formulations without finite-rate fusing cannot account correctly for the trends in the morphology and PSD. However, the small error incurred by the one-PBE model indicates that this approach is a reasonable choice for simulations where predictions of such properties are not required, as is the case for many turbulent flame simulations.

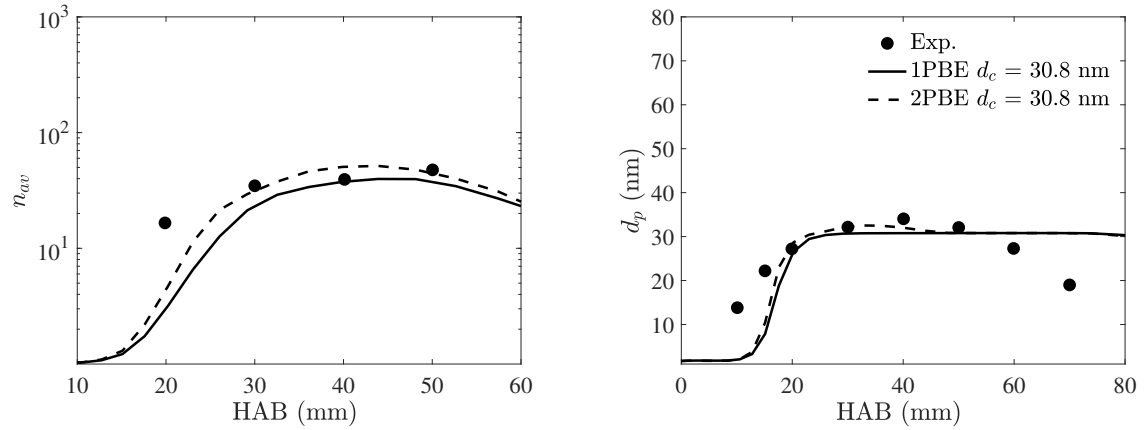
8. Conclusions

In the present study, we developed a population balance approach for modelling soot formation that distinguishes between coalescence and aggregation and incorporates finite-rate fusing of primary particles within aggregates, while providing a numerically accurate description of primary particle surface growth and oxidation within aggregates. The approach is based on the conservative finite volume PBE discretisation (CFV-1PBE) method [20], which was extended here to a two-population balance model (CFV-2PBE)



(a) Integrated soot volume fraction (b) Temperature

Figure 15: Comparison of numerical predictions by CFV-1PBE, CFV-2PBE without finite-rate fusing of primary particles and experimental data for (a) integrated soot volume fraction and (b) temperature along the centreline.



(a) n_{av} (b) d_p

Figure 16: Comparison of numerical predictions by CFV-1PBE, CFV-2PBE without finite-rate fusing of primary particles and experimental data for (a) average number of primary particles per aggregate and (b) primary particle diameter.

comprising equations for the number density of primary particles and aggregates. We also showed how the two-PBE approach can be coupled with CFD for the simulation of sooting flames.

One of the objectives for developing an accurate approach for population balance modelling is to prevent the compensation of errors between numerics and modelling. The conservative finite volume method attains accurate prediction of the distribution together with conservation of the first moment (which is proportional to mass) in aggregation. The extension to the two-PBE approach ensures that growth is calculated in a consistent manner and avoids the unphysical assumption of a cut-off point required in the one-PBE approach.

The numerical method was first shown to reproduce the self-preserving property of aggregates with varying fractal dimension. Subsequently, the CFD-PBE framework was applied to the Santoro laminar non-premixed co-flow sooting flame and the two-PBE approach was compared with the one-PBE approach. As the soot mass growth is dominated by surface growth, the surface reactivity in the HACA mechanism is critical for the soot volume fraction and it was shown that, with a properly adjusted reactivity and cut-off point, the one-PBE method is able to give a reasonably good prediction of soot volume fraction. The two-PBE approach, however, attains this result with a consistent description of growth and a more physical model for the fusing of primary particles. Furthermore, the predictions of the PSD and of the morphological parameters by the two-PBE model differed considerably from those by the one-PBE model. The lack of information on the fusing timescale, however, necessitates the extrapolation of sintering models for other nanoparticles, such as silica and titania. Models for these two nanoparticles were implemented in the context of CFV-2PBE and tested, and significant improvement in the description of soot morphology could be attained with an adjustment in the model parameters. However, it is clear that further research is warranted in this area in order to accomplish fully predictive simulations of soot aggregation. Furthermore, recent work by Goudeli et al. [80] has studied the variation of fractal dimension and this effect could also be incorporated in future work.

One of the objectives of the analysis in this paper is to lay the groundwork for the application of CFD-PBE coupling to turbulent flames, where the uncertainty involves several more factors, such as the turbulence-chemistry and turbulence-soot interaction. Given the fact that measurements in turbulent flames exist mainly for the soot volume fraction, the findings of this study demonstrate why the one-PBE approach has been used with relative success so far and is probably a reasonable choice. However, the parameter that must be adjusted in the one-PBE model (the cut-off point) is artificial and therefore, once experimental information on the fusing of soot primary particles becomes available, it should be possible to harvest the potential of the two-PBE approach towards attaining truly predictive simulations of soot formation in flames.

Acknowledgements

Binxuan Sun gratefully acknowledges the financial support by the Imperial-China Scholarship Council (CSC) scheme. This work used the Imperial College Research Computing Service (DOI: 10.14469/hpc/2232). The authors are also grateful to Prof. Dr. Sotiris E. Pratsinis for insightful discussions on sintering.

Appendix A Discretisation and validation for the convection and diffusion of primary particles

In this section, we show in detail the discretisation scheme for the convection and diffusion of primary particles and validate it via a simplified test case. Following the rationale explained in section 4.4, the transport equation for the convection and diffusion of the number density of primary particles $N_{p,i}$ in the volume section v_i is formulated as follows:

$$\frac{\partial N_{p,i}}{\partial t} + \frac{\partial u_j N_{p,i}}{\partial x_j} = \frac{\partial}{\partial x_j}\left(n_{av,i} D_{p,i} \frac{\partial N_i}{\partial x_j}\right) + S_p \tag{47}$$

where all the other terms involved in the PBE are grouped into S_p for brevity. Introducing Eq. 4, this equation can be written as follows:

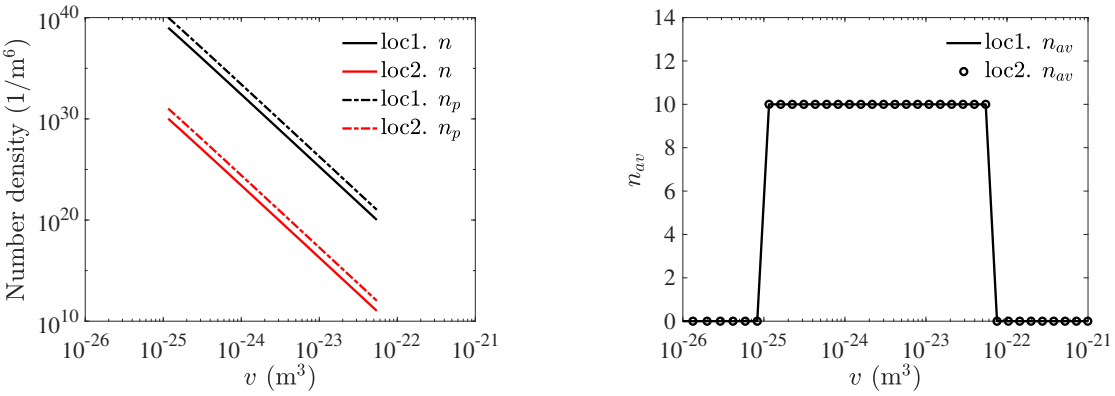
$$\frac{\partial N_{p,i}}{\partial t} + \frac{\partial u_j N_{p,i}}{\partial x_j} = \frac{\partial}{\partial x_j}\left[n_{av,i} D_{p,i} \frac{\partial}{\partial x_j}\left(\frac{N_{p,i}}{n_{av,i}}\right)\right] + S_p \tag{48}$$

We now apply the chain rule in the r.h.s. of the equation to obtain:

$$\begin{aligned}\frac{\partial N_{p,i}}{\partial t} + \frac{\partial u_j N_{p,i}}{\partial x_j} &= \frac{\partial}{\partial x_j}\left(D_{p,i}\frac{\partial N_{p,i}}{\partial x_j} - D_{p,i}\frac{N_{p,i}}{n_{av,i}}\frac{\partial n_{av,i}}{\partial x_j}\right) + S_p \\ &= \frac{\partial}{\partial x_j}\left(D_{p,i}\frac{\partial N_{p,i}}{\partial x_j}\right) - \frac{\partial}{\partial x_j}\left(D_{p,i}\frac{N_{p,i}}{n_{av,i}}\frac{\partial n_{av,i}}{\partial x_j}\right) + S_p\end{aligned} \tag{49}$$

where the second term in the r.h.s. of the equation accounts for the connection between the transport of soot aggregates and primary particles.

To test the consistency of this scheme, a test case is set up where a fuel jet containing soot aggregates is injected into air. The particle size distribution of the soot aggregate is initialised to have a linear profile. Furthermore, we assume that each soot aggregate contains 10 primary particles and the diffusion coefficient $D_{p,i}$ for each section is the same. Since soot aggregates only experience convection and diffusion process in the test case, the theoretical value for the average number of primary particles per aggregate in the domain should always remain 10 for each effective volume section. The test case undergoes 2000 time steps with $dt = 1 \times 10^{-5}$ s and the results are collected at two heights (HAB = 5 mm and 20 mm) along the centreline. Under the assumption of an identical diffusion coefficient, the correct transport of the particles via convection and diffusion should yield a PSD of the same shape at different spatial locations. This is indeed accomplished, as shown in Fig. 17a. Fig. 17b shows that, at two probe locations in the domain, each effective



(a) PSD (b) Average number of primary particles per aggregate

Figure 17: (a) PSD of soot particles, and (b) average number of primary particles per aggregates collected at two probe locations along the centreline. The black line represents location 1 at HAB 5 mm; the red line represents location 2 at HAB 20 mm.

volume section contains soot aggregates that have 10 primary particles per aggregate. Another two probes are placed in a different radial location, $r = 10$ mm, to validate the transport along the radial direction. The results are identical and not shown for brevity.

References

[1] G. Kelesidis, E. Goudeli, S. Pratsinis, Flame synthesis of functional nanostructured materials and devices: Surface growth and aggregation, Proceedings of the Combustion Institute 36 (2017) 29–50.

[2] M. Balthasar, M. Kraft, A stochastic approach to calculate the particle size distribution function of soot particles in laminar premixed flames, Combustion and Flame 133 (2003) 289–298.

[3] A. Bouaniche, J. Yon, P. Domingo, L. Vervisch, Analysis of the soot particle size distribution in a laminar premixed flame: a hybrid stochastic/fixed-sectional approach, Flow, Turbulence and Combustion 104 (2020) 753–775.

[4] M. Frenklach, S. J. Harris, Aerosol dynamics modeling using the method of moments, Journal of Colloid and Interface Science 118 (1987) 252–261.

[5] M. Frenklach, Method of moments with interpolative closure, Chemical Engineering Science 57 (2002) 2229–2239.

[6] M. E. Mueller, G. Blanquart, H. Pitsch, A joint volume-surface model of soot aggregation with the method of moments, Proceedings of the Combustion Institute 32 (2009) 785–792.

[7] R. Bleck, A fast, approximative method for integrating the stochastic coalescence equation, Journal of Geophysical Research 75 (1970) 5165–5171.

[8] F. Gelbard, Y. Tambour, J. H. Seinfeld, Sectional representations for simulating aerosol dynamics, Journal of Colloid and Interface Science 76 (1980) 541–556.

[9] M. B. Colket, R. J. Hall, Successes and uncertainties in modelling soot formation in laminar, premixed flames, in: H. Bockhorn (Ed.), Soot Formation in Combustion, Springer Series in Chemical Physics 59, Springer-Verlag, 1994, pp. 442–470.

[10] M. D. Smooke, R. J. Hall, M. B. Colket, J. Fielding, M. B. Long, C. S. McEnally, L. D. Pfefferle, Investigation of

the transition from lightly sooting towards heavily sooting co-flow ethylene diffusion flames, Combustion Theory and Modelling 8 (2004) 593–606.

[11] M. D. Smooke, M. B. Long, B. C. Connelly, M. B. Colket, R. J. Hall, Soot formation in laminar diffusion flames, Combustion and Flame 143 (2005) 613–628.

[12] S. B. Dworkin, M. D. Smooke, V. Giovangigli, The impact of detailed multicomponent transport and thermal diffusion effects on soot formation in ethylene/air flames, Proceedings of the Combustion Institute 32 (2009) 1165–1172.

[13] S. Kumar, D. Ramkrishna, On the solution of population balance equations by discretization - I. A fixed pivot technique, Chemical Engineering Science 51 (1996) 1311–1332.

[14] S. H. Park, S. N. Rogak, W. K. Bushe, J. Z. Wen, M. J. Thomson, An aerosol model to predict size and structure of soot particles, Combustion Theory and Modelling 9 (2005) 499–513.

[15] J. Wen, M. Thomson, S. Park, S. Rogak, M. Lightstone, Study of soot growth in a plug flow reactor using a moving sectional model, Proceedings of the Combustion Institute 30 (2005) 1477–1484.

[16] F. Sewerin, S. Rigopoulos, An explicit adaptive grid approach for the numerical solution of the population balance equation, Chemical Engineering Science 168 (2017) 250–270.

[17] F. Sewerin, S. Rigopoulos, An LES-PBE-PDF approach for modeling particle formation in turbulent reacting flows, Physics of Fluids 29 (2017).

[18] F. Sewerin, S. Rigopoulos, An LES-PBE-PDF approach for predicting the soot particle size distribution in turbulent flames, Combustion and Flame 189 (2018) 62–76.

[19] F. Sewerin, S. Rigopoulos, Algorithmic aspects of the LES-PBE-PDF method for modeling soot particle size distributions in turbulent flames, Combustion Science and Technology 191 (2019) 766–796.

[20] A. Liu, S. Rigopoulos, A conservative method for numerical solution of the population balance equation, and application to soot formation, Combustion and Flame 205 (2019) 506–521.

[21] S. Rigopoulos, Modelling of soot aerosol dynamics in turbulent flow, Flow, Turbulence and Combustion 103 (2019) 565–604.

[22] H. A. Michelsen, M. B. Colket, P. Bengtsson, A. D'Anna, P. Desgroux, B. S. Haynes, J. H. Miller, G. J. Nathan, H. Pitsch, H. Wang, A review of terminology used to describe soot formation and evolution under combustion and pyrolytic conditions, ACS Nano 14 (2020) 12470–12490.

[23] K. Netzell, H. Lehtiniemi, F. Mauss, Calculating the soot particle size distribution function in turbulent diffusion flames using a sectional method, Proceedings of the Combustion Institute 31 (2007) 667–674.

[24] P. Rodrigues, B. Franzelli, R. Vicquelin, O. Gicquel, N. Darabiha, Unsteady dynamics of PAH and soot particles in laminar counterflow diffusion flames, Proceedings of the Combustion Institute 36 (2017) 927–934.

[25] P. Rodrigues, B. Franzelli, R. Vicquelin, O. Gicquel, N. Darabiha, Coupling an LES approach and a soot sectional model for the study of sooting turbulent non-premixed flames, Combustion and Flame 190 (2018) 477–499.

[26] A. Liu, C. E. Garcia, F. Sewerin, B. A. O. Williams, S. Rigopoulos, Population balance modelling and laser diagnostic validation of soot particle evolution in laminar ethylene diffusion flames, Combustion and Flame 221 (2020) 384–400.

[27] W. Koch, S. K. Friedlander, The effect of particle coalescence on the surface area of a coagulating aerosol, Journal of Colloid and Interface Science 140 (1990) 419–427.

[28] Y. Xiong, S. E. Pratsinis, Formation of agglomerate particles by coagulation and sintering - Part I. A two-dimensional solution of the population balance equation, Journal of Aerosol Science 24 (1993) 283–300.

[29] Y. Xiong, M. Kamal Akhtar, S. E. Pratsinis, Formation of agglomerate particles by coagulation and sintering - Part II. The evolution of the morphology of aerosol-made titania, silica and silica-doped titania powders, Journal of Aerosol Science 24 (1993) 301–313.

[30] S. N. Rogak, Modeling small cluster deposition on the primary particles of aerosol agglomerates, Journal of Aerosol

Science 26 (1997) 127–140.

[31] S. Tsantilis, S. E. Pratsinis, Evolution of primary and aggregate particle-size distributions by coagulation and sintering, AIChE Journal 46 (2000) 407–415.

[32] J. I. Jeong, M. Choi, A sectional method for the analysis of growth of polydisperse non-spherical particles undergoing coagulation and coalescence, Journal of Aerosol Science 32 (2001) 565–582.

[33] S. H. Park, S. N. Rogak, A one-dimensional model for coagulation, sintering, and surface growth of aerosol agglomerates, Aerosol Science and Technology 37 (2003) 947–960.

[34] S. H. Park, S. N. Rogak, A novel fixed-sectional model for the formation and growth of aerosol agglomerates, Journal of Aerosol Science 35 (2004) 1385–1404.

[35] S. B. Dworkin, Q. Zhang, M. J. Thomson, N. A. Slavinskaya, U. Riedel, Application of an enhanced PAH growth model to soot formation in a laminar coflow ethylene/air diffusion flame, Combustion and Flame 158 (2011) 1682–1695.

[36] A. Veshkini, S. B. Dworkin, M. J. Thomson, A soot particle surface reactivity model applied to a wide range of laminar ethylene/air flames, Combustion and Flame 161 (2014) 3191–3200.

[37] A. Khosousi, S. B. Dworkin, Soot surface reactivity during surface growth and oxidation in laminar diffusion flames, Combustion and Flame 162 (2015) 4523–4532.

[38] N. A. Eaves, Q. Zhang, F. Liu, H. Guo, S. B. Dworkin, M. J. Thomson, Coflame: A refined and validated numerical algorithm for modeling sooting laminar coflow diffusion flames, Computer Physics Communications 207 (2016) 464–477.

[39] A. Veshkini, S. B. Dworkin, M. J. Thomson, Understanding soot particle size evolution in laminar ethylene/air diffusion flames using novel soot coalescence models, Combustion Theory and Modelling 20 (2016) 707–734.

[40] D. Chen, Z. Zainuddin, E. Yapp, J. Akroyd, S. Mosbach, M. Kraft, A fully coupled simulation of pah and soot growth with a population balance model, Proceedings of the Combustion Institute 34 (2013) 1827–1835.

[41] R. J. Santoro, H. G. Semerjian, R. A. Dobbins, Soot particle measurements in diffusion flames, Combustion and Flame 51 (1983) 203–218.

[42] S. K. Friedlander, Smoke, Dust, and Haze: Fundamentals of Aerosol Dynamics, 2nd ed., Oxford University Press, 2000.

[43] Q. Zhang, M. J. Thomson, H. Guo, F. Liu, G. J. Smallwood, A numerical study of soot aggregate formation in a laminar coflow diffusion flame, Combustion and Flame 156 (2009) 697–705.

[44] C. Saggese, S. Ferrario, J. Camacho, A. Cuoci, A. Frassoldati, E. Ranzi, H. Wang, T. Faravelli, Kinetic modeling of particle size distribution of soot in a premixed burner-stabilized stagnation ethylene flame, Combustion and Flame 162 (2015) 3356–3369.

[45] U. O. Köylü, C. S. McEnally, D. E. Rosner, L. D. Pfefferle, Simultaneous measurements of soot volume fraction and particle size / microstructure in flames using a thermophoretic sampling technique, Combustion and Flame 110 (1997) 494–507.

[46] A. M. Brasil, T. L. Farias, M. G. Carvalho, A recipe for image characterization of fractal-like aggregates, Journal of Aerosol Science 30 (1999) 1379–1389.

[47] O. Link, D. R. Snelling, K. A. Thomson, G. J. Smallwood, Development of absolute intensity multi-angle light scattering for the determination of polydisperse soot aggregate properties, Proceedings of the Combustion Institute 33 (2011) 847–854.

[48] M. Schenk, S. Lieb, H. Vieker, A. Beyer, A. Gölzhäuser, H. Wang, K. Kohse-Höinghaus, Morphology of nascent soot in ethylene flames, Proceedings of the Combustion Institute 35 (2015) 1879–1886.

[49] B. Koren, A robust upwind discretization method for advection, diffusion and source terms, in: C. B. Vreugdenhil, B. Koren (Eds.), Numerical Methods for Advection-Diffusion Problems, volume 45 of *Notes on Numerical Fluid Mechanics and Multidisciplinary Design*, Vieweg Verlag, 1993, pp. 117–138.

[50] S. Qamar, M. P. Elsner, I. A. Angelov, G. Warnecke, A. Seidel-Morgenstern, A comparative study of high resolution

schemes for solving population balances in crystallization, Computers and Chemical Engineering 30 (2006) 1119–1131.

[51] S. Qamar, G. Warnecke, M. P. Elsner, On the solution of population balances for nucleation,growth,aggregation and breakage processes, Chemical Engineering Science 64 (2009) 2088–2095.

[52] N. H. Qamar, Z. T. Alwahabi, Q. N. Chan, G. J. Nathan, D. Roekaerts, K. D. King, Soot volume fraction in a piloted turbulent jet non-premixed flame of natural gas, Combustion and Flame 156 (2009) 1339–1347.

[53] W. P. Jones, F. di Mare, A. J. Marquis, LES-BOFFIN: user's guide, 2002.

[54] G. Blanquart, P. Pepiot-Desjardins, H. Pitsch, Chemical mechanism for high temperature combustion of engine relevant fuels with emphasis on soot precursors, Combustion and Flame 156 (2009) 588–607.

[55] G. Blanquart, H. Pitsch, A joint volume-surface-hydrogen multi-variate model for soot formation, in: H. Bockhorn, A. D'Anna, A. Sarofim, H. Wang (Eds.), Combustion Generated Fine Carbonaceous Particles, KIT Scientific Publishing, 2009, pp. 437–463.

[56] M. Frenklach, H. Wang, Detailed mechanism and modeling of soot particle formation, in: H. Bockhorn (Ed.), Soot Formation in Combustion, Springer Series in Chemical Physics 59, Springer-Verlag, 1994, pp. 162–192.

[57] S. J. Harris, I. M. Kennedy, The coagulation of soot particles with van der waals forces, Combustion Science and Technology 59 (1988) 443–454.

[58] C. Marchal, Soot formation and oxidation modelling in an automotive engine, Ph.D. thesis, Université d'Orléans, 2008.

[59] M. Frenklach, H. Wang, Detailed modeling of soot particle nucleation and growth, Symposium (International) on Combustion 23 (1991) 1559–1566.

[60] H. Guo, F. Liu, G. J. Smallwood, O. L. Gülder, Numerical study on the influence of hydrogen addition on soot formation in a laminar ethylene–air diffusion flame, Combustion and Flame 145 (2006) 324–338.

[61] J. Appel, H. Bockhorn, M. Frenklach, Kinetic modeling of soot formation with detailed chemistry and physics: Laminar premixed flames of C2 hydrocarbons, Combustion and Flame 121 (2000) 122–136.

[62] S. E. Pratsinis, Simultaneous nucleation, condensation, and coagulation in aerosol reactors, Journal of Colloid and Interface Science 124 (1988) 416–427.

[63] A. Kazakov, M. Frenklach, Dynamic modeling of soot particle coagulation and aggregation: Implementation with the method of moments and application to high-pressure laminar premixed flames, Combustion and Flame 114 (1998) 484–501.

[64] S. Tsantilis, H. Briesen, S. E. Pratsinis, Sintering time for silica particle growth, Journal of Aerosol Science 34 (2001) 237–246.

[65] A. Kobata, K. Kusakabe, S. Morooka, Growth and transformation of TiO_2 crystallites in aerosol reactor, AIChE Journal 37 (1991) 347–359.

[66] E. Goudeli, M. L. Eggersdorfer, S. E. Pratsinis, Aggregate characteristics accounting for the evolving fractal-like structure during coagulation and sintering, Journal of Aerosol Science 89 (2015) 58–68.

[67] S. Vemury, S. E. Pratsinis, Self-preserving size distributions of agglomerates, Journal of Aerosol Science 26 (1995) 175–185.

[68] S. K. Friedlander, C. S. Wang, The self-preserving particle size distribution for coagulation by Brownian motion, Journal of Colloid and Interface Science 22 (1966) 126–132.

[69] R. J. Santoro, T. T. Yeh, J. J. Horvath, H. G. Semerjian, The transport and growth of soot particles in laminar diffusion flames, Combustion Science and Technology 53 (1987) 89–115.

[70] C. M. Megaridis, R. A. Dobbins, Comparison of soot growth and oxidation in smoking and non–smoking ethylene diffusion flames, Combustion Science and Technology 66 (1989) 1–16.

[71] S. S. Iyer, T. A. Litzinger, S. Y. Lee, R. J. Santoro, Determination of soot scattering coefficient from extinction and three-angle scattering in a laminar diffusion flame, Combustion and Flame 149 (2007) 206–216.

[72] Q. Zhang, H. Guo, F. Liu, G. J. Smallwood, M. J. Thomson, Modeling of soot aggregate formation and size distribution in a laminar ethylene/air coflow diffusion flame with detailed PAH chemistry and an advanced sectional aerosol dynamics

model, Proceedings of the Combustion Institute 32 (2009) 761–768.

[73] H. Guo, F. Liu, G. J. Smallwood, Gülder, Ö. L., The flame preheating effect on numerical modelling of soot formation in a two-dimensional laminar ethylene–air diffusion flame, Combustion Theory and Modelling 6 (2002) 173–187.

[74] J. D. Landgrebe, S. E. Pratsinis, A discrete-sectional model for particulate production by gas-phase chemical reaction and aerosol coagulation in the free-molecular regime, Journal of Colloid and Interface Science 139 (1990) 63–86.

[75] I. M. Kennedy, C. Yam, D. C. Rapp, R. J. Santoro, Modeling and measurements of soot and species in a laminar diffusion flame, Combustion and Flame 107 (1996) 368–382.

[76] P. Akridis, S. Rigopoulos, Modelling of soot formation in laminar diffusion flames using a comprehensive CFD-PBE model with detailed gas-phase chemistry, Combustion Theory and Modelling 21 (2017) 35–48.

[77] R. Puri, T. F. Richardson, R. J. Santoro, R. A. Dobbins, Aerosol dynamic processes of soot aggregates in a laminar ethene diffusion flame, Combustion and Flame 92 (1993) 320–333.

[78] D. Chen, K. Luo, Reactive sites on the surface of polycyclic aromatic hydrocarbon clusters: A numerical study, Combustion and Flame 211 (2020) 362–373.

[79] G. A. Kelesidis, S. E. Pratsinis (in press), Determination of the volume fraction of soot accounting for its composition and morphology, Proceedings of the Combustion Institute (2020).

[80] E. Goudeli, M. L. Eggersdorfer, S. E. Pratsinis, Coagulation–agglomeration of fractal-like particles: structure and self-preserving size distribution, Langmuir 31 (2015) 1320–1327.